

JGR Solid Earth

RESEARCH ARTICLE

10.1029/2021JB023867

Key Points:

- Saturation obtained by drainage and imbibition methods lead to different dispersion and attenuation of elastic-wave velocities
- Experimental results on the attenuation and dispersion highlight the importance of the fluid distribution which was investigated using computer-assisted tomographic (CT)
- A numerical model based on Biot's theory using the fluid distribution—from the CT scan as an input—reproduces the experimental results

Correspondence to:

S. Wang and C. Sun,
wangsx@cup.edu.cn;
kang2008ping2008@163.com






Citation:

Sun, C., Fortin, J., Borgomano, J. V. M., Wang, S., Tang, G., Bultreys, T., & Cnudde, V. (2022). Influence of fluid distribution on seismic dispersion and attenuation in partially saturated limestone. *Journal of Geophysical Research: Solid Earth*, 127, e2021JB023867. <https://doi.org/10.1029/2021JB023867>

Received 21 DEC 2021

Accepted 18 APR 2022

Influence of Fluid Distribution on Seismic Dispersion and Attenuation in Partially Saturated Limestone

Chao Sun^{1,2} , Jérôme Fortin², Jan V. M. Borgomano^{2,3} , Shangxu Wang^{4,5} , Genyang Tang^{4,5}, Tom Bultreys⁶ , and Veerle Cnudde^{6,7} 

¹College of Resources and Geoscience, China University of Mining and Technology, XuZhou, China, ²Laboratoire de Géologie, Ecole Normale Supérieure/CNRS, PSL Research University, Paris, France, ³MODIS Pau, Pau, France, ⁴State Key Laboratory of Petroleum Resources and Prospecting, China University of Petroleum, Beijing, China, ⁵Key Laboratory of Geophysical Prospecting, CNPC, Beijing, China, ⁶Department of Geology, PProGRess/UGCT, Ghent University, Ghent, Belgium, ⁷Department of Earth Sciences, Environmental Hydrogeology Group, Utrecht University, Utrecht, The Netherlands

Abstract Quantitatively assessing attenuation and dispersion of elastic-wave velocities in partially saturated reservoir is difficult because of its sensitivity to fluid distribution. We conducted experiments on homogeneous Indiana limestone samples, partially saturated by two methods: drying and imbibition which lead to different fluid distribution for a given saturation. Forced oscillations (from 0.004 to 100 Hz) and ultrasonic (1 MHz) measurements were done under confining pressure to measure the change of elastic moduli with frequency and their attenuation. Our measurements show that compressional (P-)velocities are strongly sensitive to the sample's saturation method. For high saturations (above 80%), obtained by drainage, compressional velocities are frequency dependent, and clear peaks of attenuation can be observed. However, at the same saturations obtained by imbibition, no dispersion or attenuation is observed. In addition, shear velocities show little variation with frequency, saturations, and fluid distribution. The dispersion and attenuation of P-velocities are shown to be influenced by the pore fluid distribution, which was investigated using micro-computer-assisted tomographic (CT) scans. Furthermore, a numerical model developed within the framework of poroelasticity's theory predicts well the experimental results, using the fluid distribution obtained from CT as an input. Our results show that the velocity dispersion was related to wave-induced fluid flow at mesoscopic scale controlled by the geometry and distribution of the gas patches.

Plain Language Summary It is difficult to quantitatively assess frequency-dependent elastic-wave velocities in partially saturated reservoir, due to its sensitivity to fluid distribution. The topic of our study aims at investigating the effect of fluid distribution on frequency-dependent elastic velocities using rock-physics experiments. In the experiments, dispersion and attenuation curves observed for a water–air-saturated porous limestone exhibited distinct variations for the same saturation. The variations were proved to be related to different saturation methods, thus providing physical evidence of the effect of fluid distribution on the frequency-dependent elastic velocities. Furthermore, micro-computer-assisted tomographic scan was used to calculate the fluid distributions from different saturation methods. The scanned fluid distributions, as the inputs of poroelastic model, were able to interpret the dispersion and attenuation observed. The conclusion provides the possibility to quantify the relationship between fluid distribution and seismic attenuation and could be a useful tool for upscaling at reservoir scale. In addition, the study improves our understanding of seismic wave propagation in partially fluid-saturated rock formations and thus has potential applications in seismic exploration, reservoir production, and for CO₂ sequestration in aquifers.

1. Introduction

The detection and the characterization of fluid saturation and fluid distribution are important research topics in seismic exploration, during reservoir production, and for CO₂ sequestration in aquifers. Since partially saturated reservoirs are usually heterogeneous at a mesoscopic scale, which is smaller than the seismic wave length (Müller et al., 2010), it is difficult to directly identify the fluid distribution or its corresponding fluid saturation using macroscopic methods, such as migration-imaging technology of field data. However, when seismic waves propagate in fluid-saturated reservoirs, dispersion and attenuation related to wave-induced fluid flow (WIFF) may occur depending on the fluid distribution or the fluid saturation (Müller et al., 2010; Pride et al., 2004; Solazzi et al., 2019). In WIFF theory, various mechanisms regarding partial saturation are well documented and

have been analytically and numerically explored for idealized scenarios: the 1D-layered model (Qi, Tobias, & Boris, 2014; White et al., 1975), the spherical model (Dutta & Odé, 1979), and for a fractal pore fluid distribution (Müller et al., 2008; Qi, Tobias, & Germán, 2014; Rubino & Holliger, 2013; Rubino et al., 2009). These theoretical predictions show that the magnitude and frequency dependence of the seismic attenuation are strongly dependent on the degree of saturation, on the fluid distribution, as well as on the physical properties of the pore fluid (i.e., viscosity and compressibility). To validate the underlying physical models, direct observations of dispersion and attenuation in the seismic frequency range are essential. Domenico (1976) measures the nonlinear variation of P wave velocity in an unconsolidated gas-saturated sand with increasing brine saturation. The velocity measurements were well approached by the Geertsma (1961)'s expression at low brine saturation, while they had a significant mismatch at high brine saturation. They argue that the difference is related to the distribution of the gas-brine mixture in the pore space: sufficiently uniform at low saturations but nonuniform at high saturations. Spencer (1981) develops a stress-strain apparatus to investigate the frequency-dependent seismic attenuation between 4 and 400 Hz for partially fluid-saturated sandstones and finds that the dispersion and attenuation show different dependency on saturation. To explore this further, Cadoret et al. (1995) investigates a partially saturated limestone at sonic frequency (around 1 kHz). Drainage and pseudo-imbibition are used in their experiment to saturate the limestone with water. A computer-assisted tomographic (CT) scanner is used to obtain insight into the fluid distribution and it is found that the fluid distribution is homogeneous at the millimetric scale at all saturations during imbibition, whereas the fluid distribution is heterogeneous at high water saturation during drainage. Cadoret et al. (1995) find that the P wave velocity was strongly influenced by the water saturation between approximately 60% and 100% during a drainage experiment, while this is not the case for an imbibition experiment. Their experiments provide a strong evidence that the fluid distribution has a significant influence on elastic velocities. However, they are not able to capture the seismic dispersion and attenuation varying with the fluid saturation due to the limit of the resonant bar technique. In a more recent study, Spencer and Shine (2016) investigate the effects of viscosity and permeability on modulus dispersion and attenuation in sandstones as well as the effects of partial gas or oil saturation on velocities and attenuations. They conclude that the modulus dispersion and attenuations in partially saturated sandstones meet the mesoscopic WIFF theories while in fully saturated sandstones dispersion and attenuation are caused by local-flow mechanism. However, in their measurement, the estimated patch size is on the order of 10^{-1} m, which is slightly larger than the length of the sample. Therefore, it is probable that the measured dispersion and attenuation is related to “dead volume” (Pimienta et al., 2016; Sun et al., 2019). Tisato and Quintal (2013) and Tisato and Madonna (2012) investigate the dependence of attenuations on frequencies (0.1–100 Hz) at different water saturations in a Berea sandstone and numerically interpreted their observations using Biot's poroelastic equation. Their experiments and numerical solutions provide a stronger experimental evidence that the WIFF can cause dispersion and attenuation. However, there are no significant attenuation peaks observed in their measurement band (1–100 Hz) and the confining pressure in their experiment was 0.25 MPa, which does not meet reservoir conditions. To overcome previous limitations, Chapman et al. (2016) conduct an experiment on a Berea sandstone, which provides a significant attenuation peak in their measurement band (0.5–50 Hz) in a range of significantly higher confining pressures (2–25 MPa). However, their experiment has three important limitations: (a) the measurement band (0.5–50 Hz) is relatively narrow, (b) they observed a peak at a saturation of 99% with an error bar of $\pm 1\%$, and (c) the fluid distribution is unknown.

In this paper, a carefully designed experiment was conducted to investigate the attenuation and dispersion related to patchy saturation. An Indiana limestone was selected with the permeability of 0.02 mD and porosity of 10.8%. This was done because this specimen has the two following characteristics: (a) no squirt-flow was observed in fully saturated sample (Borgomano et al., 2019) and (b) the low permeability induces a very low cutoff frequency for the drained/undrained transition. In addition, we tested undrained boundary conditions in our experiment to avoid any influence of the drained/undrained transition due to the “dead volume” caused by the fluid inlet and outlet lines connecting to the both ends of the sample (Borgomano et al., 2020). Two saturation methods, imbibition and drainage/drying, were used to produce different fluid distributions, which was also investigated using X-ray CT. Finally, a numerical model in the frame of the Biot theory, combining with the X-ray CT scanning results, was built to interpret the measured dispersion and attenuation.

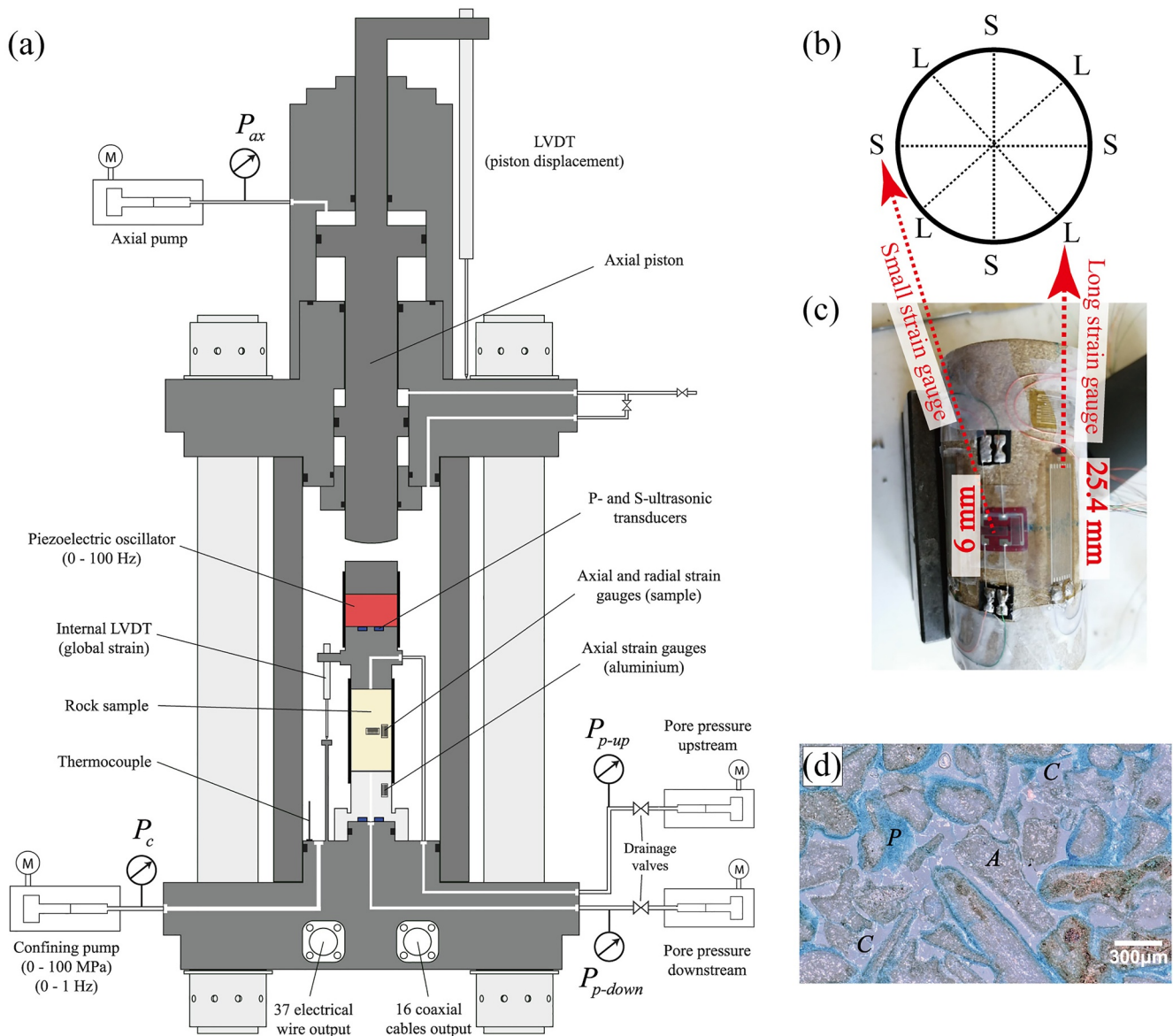


Figure 1. Schematic diagram (a) of the experimental apparatus. The hydrostatic oscillations are generated by the confining pressure pump and the axial oscillations by the piezoelectric actuator. P and S ultrasonic transducers are installed in the top and bottom end-platens. Drained or undrained boundary conditions can be achieved using microvalves. (b, c) The positions of the long (N2A-06-10CBE-350, 25.4 mm) and small strain gauges (TML FCB-6-350-11, 6 mm). (d) A picture of a thin section under reflected light microscope. Pore (P), allochems (A), and calcitic cement (C) are marked in the image. The porosity is saturated with a blue colorant in the thin section.

2. Methodology

2.1. Experimental Apparatus

2.1.1. Seismic Dispersion

The apparatus used in our experiment, installed in Ecole Normale Supérieure of Paris (Figure 1a), is an auto-compensated cell from Top Industrie with an autonomous piston. Six single-screw pumps are used to control the confining pressure (maximum of 100 MPa), axial stress, and fluid pressure (two pumps are filled with glycerin and two pumps are filled with water). The apparatus is able to measure the Young's modulus and Poisson's ratio of the sample at different frequencies using a piezoelectric oscillator (Borgomano et al., 2020). The diameter and length of the cored rock sample are 40 mm and around 80 mm, respectively, and the sample is held between both end-platens. The material of the bottom end-platen is aluminum 2017A (AU4G), with four axial-strain gauges

that are used to precisely determine the axial stress (Figure 1a). The sample is jacketed using a neoprene jacket to (a) isolate pore fluid from confining oil and (b) to prevent the dispersion and attenuation caused by lateral flow (Spencer, 1981). Moreover, ultrasonic transducers (P and S) are embedded in both end-platens, in order to measure the ultrasonic (1 MHz) V_p and V_s velocities. Two pumps are connected to the both end-platens to control the pore pressure inside the sample. They can also be used to measure the permeability based on Darcy's law. In addition, there are two piloted microvalves installed in the end-platens that enable to achieve, when they are closed, perfectly undrained conditions around the sample.

In our experiment, two pairs of small axial-strain and radial strain gauges (TML FCB-6-350-11, 6 mm) and four long axial-strain gauges (Micro Measurements, N2A-06-10CBE-350, 25.4 mm) were pasted at the middle-height of the sample. The resistance of these strain gauges was 350 Ω . The details are shown in Figure 1b, where "L" represents the long strain gauge and "S" represents the small strain gauge. All the measurements were conducted under the differential ($P_c - P_p$) pressure of 5 MPa.

2.2. Forced-Oscillations Method

The Young's modulus and attenuation can be calculated using Equations 1 and 2:

$$E = E_{al} * \epsilon_{al} / \epsilon_{ax} \quad (1)$$

And

$$Q_E^{-1} = \tan(\varphi_{al} - \varphi_{ax}) \quad (2)$$

where the E_{al} is the Young's modulus of the bottom aluminum-end-platen; ϵ_{al} is the axial strain of the end-platen; ϵ_{ax} is the axial strain of the sample; and φ_{al} and φ_{ax} are the axial-strain phases of the aluminum reference and the sample. In addition, the Poisson's ratio ν and the phase difference Q_ν^{-1} are calculated using formulas 3 and 4:

$$\nu = \epsilon_{ra} / \epsilon_{ax} \quad (3)$$

And

$$Q_\nu^{-1} = \tan(\varphi_{ax} - \varphi_{ra}) \quad (4)$$

where ϵ_{ra} is the amplitude of the radial strain of the sample and φ_{ra} is the phase of the radial strain. In our experiment, the strain signal measured by the strain gauges will be averaged to calculate the Young's moduli and Poisson's ratio.

Assuming that the sample is isotropic, K and G can be estimated using the following formulas 5 and 6:

$$K = \frac{E}{3(1-2\nu)} \quad (5)$$

And

$$G = \frac{E}{2(1+\nu)} \quad (6)$$

The shear attenuation Q_G^{-1} can be calculated using Q_E^{-1} and Q_ν^{-1} based on the relationship (e.g., Borgomano et al., 2017; Mavko & Mukerji, 1998; Winkler & Nur, 1979):

$$Q_\nu^{-1} [v + Q_G^{-1} ((1+\nu)Q_E^{-1} - Q_G^{-1})] = (1+\nu)Q_E^{-1} - (1+\nu)Q_G^{-1} \quad (7)$$

Then, we calculated Q_K^{-1} with the relationship from Winkler and Nur (1979) using Q_E^{-1} , Q_G^{-1} , and ν :

$$Q_K^{-1} = \frac{3}{1-2\nu} Q_E^{-1} - \frac{2(1+\nu)}{1-2\nu} Q_G^{-1} \quad (8)$$

Table 1
Properties of the Indiana Limestone, Water, and Air

Name properties	Indiana	Water	Air
Porosity, ϕ (%)	10.8	–	–
Length, L (mm)	81.0	–	–
Diameter, D (mm)	39.7	–	–
Permeability (m^2)	2×10^{-17}	–	–
Bulk modulus, K_{dry} (GPa)	25 ($P_c = 5$ MPa)	2.25	1×10^{-4}
Density, ρ (kg m^{-3})	2,369.2	1,000	1
Viscosity, η (mPa s)	–	10^{-3}	2×10^{-5}

Note. The bulk modulus is measured at the confining pressure of 5 MPa ($P_c = 5$ MPa).

2.3. Bioclastic Limestone From Indiana

Indiana limestone (Figure 1c) is a pure calcite bioclastic limestone (Fossum et al., 1995). It may also be known as the Salem or Spergen limestone. Many researchers have investigated its mechanical properties (Hart & Wang, 1995; Ji et al., 2012; Michalopoulos & Triandafilidis, 1976; Vajdova et al., 2004; Zhu et al., 2010). The Indiana limestone sample was cored from the same block as the one used in Borgomano et al. (2019). The porosity of the sample was measured by the triple-weight method and it was found to be 10.8%. The Indiana limestone consists of clasts (fossil fragments and ooids) and calcite cement resulting in range of grain sizes from less than 5 μm for the cement to 300 μm for an average-sized fossils. The density of the sample is 2,369.2 kg/m^3 . The optical micrograph (Figure 1d) did not show visible microcracks, which is in line with the absence of squirt-flow mechanism in the dispersion measurements of Borgomano et al. (2019). The permeability measured at a differential pressure ($P_c - P_p$) of 5 MPa is $2 \times 10^{-17} \text{ m}^2$. Petrophysical properties of the sample are presented in Table 1.

2.4. Saturation Methods

Imbibition and drainage methods were used as the saturation methods, and the water saturation was monitored by regularly weighing the sample.

2.4.1. Imbibition

The protocol is as follows: the dry sample is first put in contact with water, on one side, to allow spontaneous imbibition as shown in Figures 2a–2c. The degree of saturation obtained by spontaneous imbibition is related to the petrophysical characteristics of the rock (Hirschwald, 1912) and reaches for this sample values in the range of 30%–40% after 5 hr. The saturation was calculated using the difference of the weight between the dry and partially saturated sample. To reach higher saturation, the sample is turned upside down to continue the imbibition from the other face, which generally results in final saturations in the range of 60%–88%. After imbibition, the sample is covered by a plastic film to avoid evaporation and is put in the fridge to let the capillary forces equilibrate. For the saturation of 94%, we put the bottom end of the sample at the position under the water surface of 2.5 cm for 4 hr, then flip the sample and place the top end of the sample at a position 2.5 cm underwater for again 4 hr. Then, the sample is put in the fridge. The full saturation was achieved at the end, after the measurements on the partial saturations, by flushing water through the sample in the triaxial cell.

2.4.2. Drainage

Drainage is achieved by drying the sample under ambient conditions, the steps are the followings: (a) leave the fully saturated sample under room condition (28°C) for 1 day (around 12–15 hr) this leads to a saturation of 92%. (b) Repeat the step (a), to decrease the saturation to 89%, 87%, and 78%.

2.5. X-Ray CT Scanning

To investigate the fluid distribution, the samples were scanned using the HECTOR micro-CT scanner at Ghent University's Centre for X-ray Tomography (Belgium; Masschaele et al., 2013). Subsections of the samples (indicated by the red rectangle in Figure 3) were scanned in a field of view of 3.4 cm with a voxel resolution of $0.022 \times 0.022 \times 0.022 \text{ mm}^3$. The CT scans were done ex situ on the dry and fully saturated sample and on the partially saturated sample obtained by imbibition and drainage. The overall scanning size is $\varnothing 40 \text{ mm} \times L 38.4 \text{ mm}$. Before the scanning, KI (iodide of potassium) was dissolved in the pore fluid to increase the X-ray attenuation contrast between air and brine. It should be noted that the salinity of the fluid is not higher than 4 wt%, in order to prevent crystallization phenomena during the drying process. The samples were wrapped in plastic foil to avoid drying during the scans.

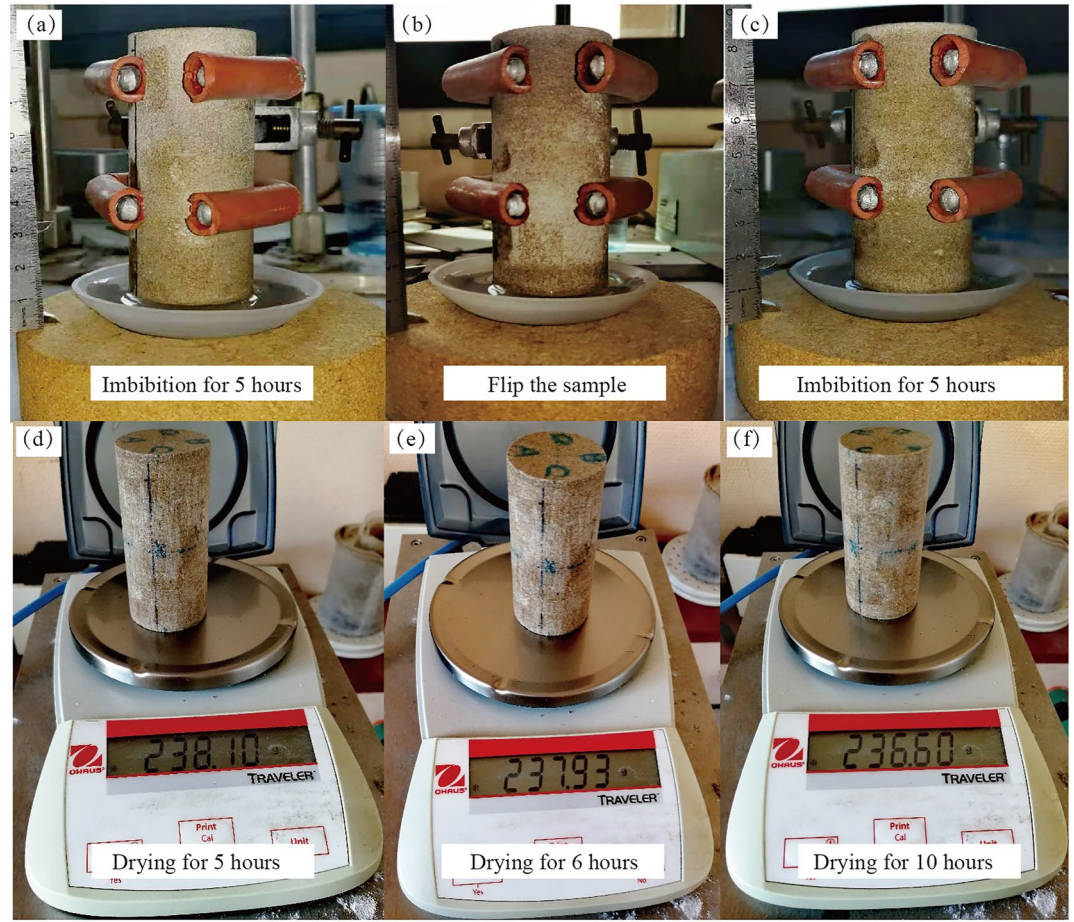


Figure 2. The process of sample saturated with water using imbibition (a–c) and drying (d–f).

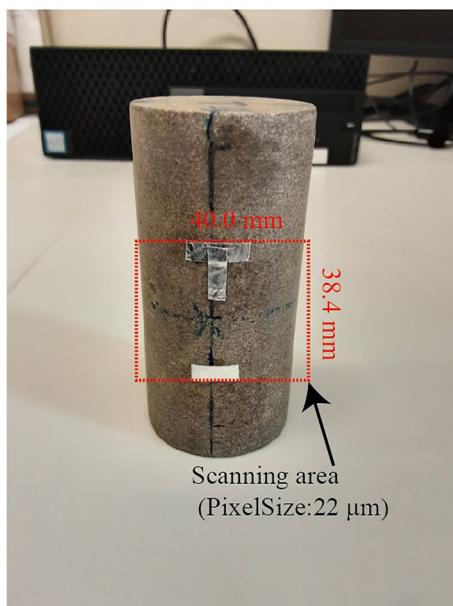


Figure 3. CT scanning volume with a volume resolution of $0.022 \times 0.022 \times 0.022 \text{ mm}^3$.

The CT scanning results can be used to estimate the porosity and fluid distribution, following the methodology given in Cadoret et al. (1995), Akin and Kovscek (2003), and Chapman et al. (2021, 2022). The preprocessing steps are the followings: (a) we first normalized the image of the fully saturated sample to the dry sample, using the “Normalize Grayscale” model in Avizo (Lin et al., 2017); (b) in a second step, we made a difference between the gray values in the images of the fully water-saturated sample and the dry sample, that is, $CT_{Water} - CT_{Air}$; and (c) the porosity distribution is obtained as

$$\phi = \frac{CT_{Water} - CT_{Air}}{\Theta} \quad (9)$$

where Θ refer to the normalization coefficient.

The gas (air) saturation, S_{Air} , is estimated using the formula:

$$S_{Air} = \frac{CT_{water} - CT_{water+air}}{CT_{water} - CT_{air}} \quad (10)$$

where $CT_{water+air}$ refers to gray values in the image of a partially saturated rock (including both water and air phases). During the calculation, we coarsen the voxel resolution from $0.022 \times 0.022 \times 0.022 \text{ mm}^3$ to $0.176 \times 0.176 \times 0.176 \text{ mm}^3$. The coarsening process is used to (a) reduce the data size to accelerate the calculation speed; (b) to achieve a representative

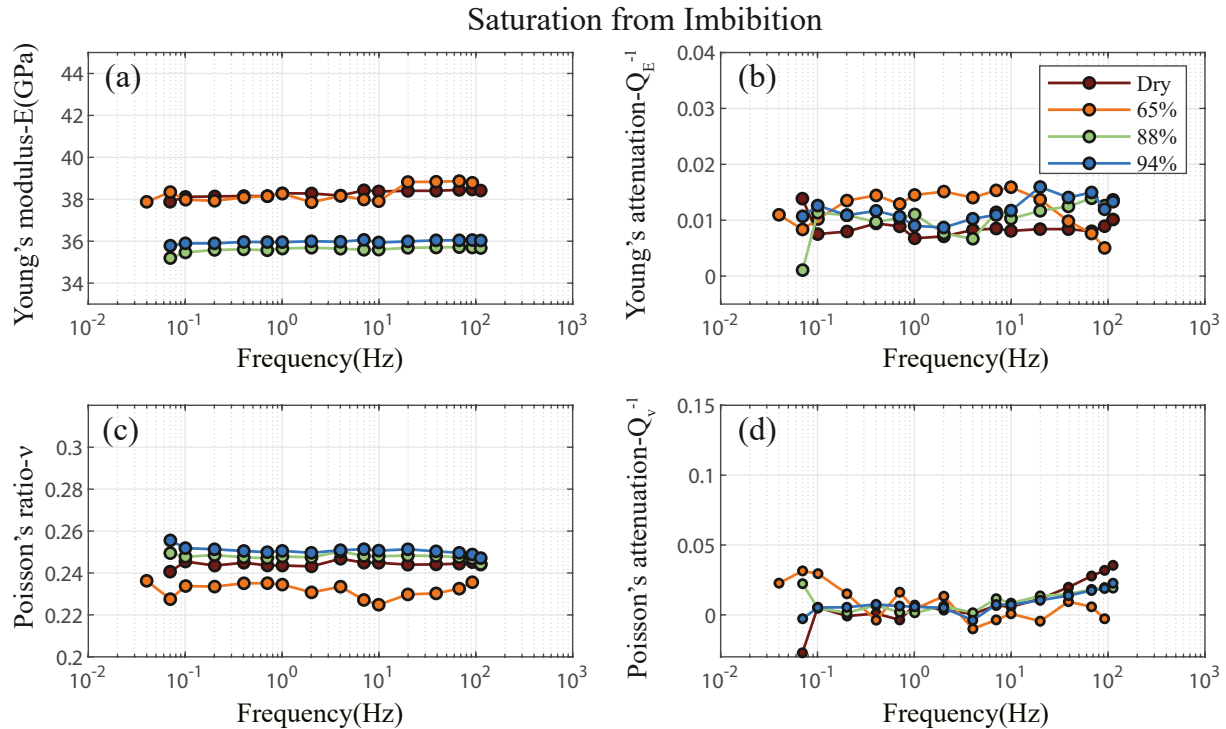


Figure 4. Young’s modulus (a), Young’s attenuation (b), Poisson’s ratio (c), and Poisson’s attenuation (the phase difference between the radial strain and the axial strain) measured using the oscillation method as the water saturation increases from dry to 94% by imbibition method. The relative uncertainty of the Young’s modulus is around 5%, and the relative uncertainty on Poisson’s ratio is around 4%.

elementary volume (REV), in which porosity and gas saturation are determined, reducing the error in these properties (Chapman et al., 2021).

3. Results and Analysis

3.1. Measurements From Imbibition Method

This section presents the frequency-dependent Young’s moduli (E and Q_E^{-1}) and Poisson’s ratio (ν and Q_ν^{-1}) when the sample is saturated using the imbibition technique. The measurements are shown in Figure 4. The relative uncertainties on E and ν were found to be around $\Delta E/E = 5\%$, $\Delta \nu/\nu = 4\%$, which correspond to 1.8 GPa for E and 0.01 for ν . Overall, there is no dispersion (Figures 4a and 4c) and attenuation (Figures 4b and 4d) in both Young’s modulus and Poisson’s ratio for all the water saturations (dry to 94%) in the seismic band [0.01–100 Hz]. In addition, the increase of the saturation from 65% to 88% seems to result in the decrease of the Young’s modulus (Figure 4a) from 38 to 36 GPa and the increase of the Poisson’s ratio (black and dark blue circles in Figure 4c) from 0.24 to 0.25. A slight decrease of Young’s modulus and shear modulus (Figure 5) with saturation has been reported in several studies (Cadoret, 1993; Geremia et al., 2021; Knight & Dvorkin, 1992; Murphy, 1982; Tiennot & Fortin, 2020; Tutuncu, 1992; Yin et al., 2019). This effect might be due to water weakening (Geremia et al., 2021) and is not predicted in the classical framework of the poroelasticity which assumes a constant shear modulus.

Using the Young’s moduli (E and Q_E^{-1}) and Poisson’s ratio (ν and Q_ν^{-1}), we can deduce the S wave moduli (G and Q_G^{-1}) and bulk moduli (K and Q_K^{-1}), which are shown in Figure 5. Propagating the uncertainties of E and ν to K and G , we obtained a relative uncertainty of 6.4% for K and G , which correspond to 1.6 GPa for K and 0.9 GPa for G . In addition, ultrasonic measurements are plotted in Figure 5 with an uncertainty of 2% for K and G . For the dry sample, there is no dispersion for G and K and these data are consistent with the ultrasonic measurements. For the partially saturated sample, there is no dispersion for all the moduli in seismic frequencies [0.01–100 Hz]. However, there is an offset between the low-frequency measurement and ultrasonics as the saturation increases: G obtained from ultrasonic measurements has no change and K increases from 25 to 32 GPa as the saturation

Saturation from Imbibition

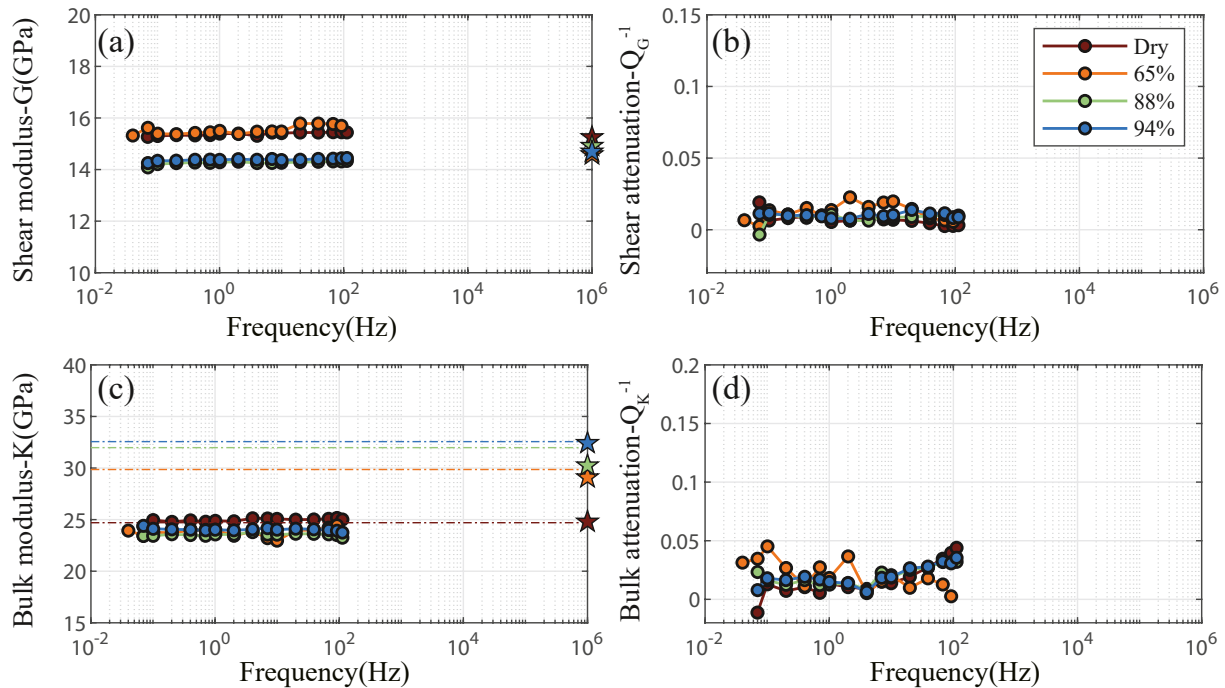


Figure 5. *S* wave modulus (a), *S* wave attenuation (b), bulk modulus (c), and bulk attenuation (d) are deduced from Figure 4. The circles are the low-frequency measurement and the stars are the ultrasonic measurements. The colorful dash lines are the Gassmann–Hill predictions at water saturations of 0%, 65%, 88%, and 94%. The relative uncertainties of (a)–(d) are around 6.4%.

increases from 65% to 94%. Another result is highlighted in Figure 5: in seismic frequencies [0.01–100 Hz], as the water saturation increases from dry to 94%, the shear modulus *G* decreases from 15.2 to 14.2 GPa, whereas the bulk modulus *K* remains almost constant.

3.2. Measurements From Drainage

Figures 6a and 6b present the frequency-dependent Young’s modulus and attenuation at different water saturations achieved by the drainage process. The relative uncertainty on *E* is around $\Delta E/E = 5\%$, that is 1.8 GPa for *E*. For saturation lower than 75%, the Young’s modulus is constant as frequency increases from 0.01 to 100 Hz, remaining at the 37–38 GPa and the corresponding Young’s attenuation is negligible regarding the error bar. However, as the water saturation increases from 75% to 99%, there is an obvious dispersion: at a saturation of 92%, the Young’s modulus increases from 37.5 to 40 GPa as the frequencies increase from 0.1 to 100 Hz. The corresponding Young’s attenuation behaves consistently with the dispersion of the Young’s modulus: the attenuation peaks appear at a frequency of 20–100 Hz, moving toward lower frequency as the saturation increases. In addition, the magnitude of the Young’s attenuation is maximum at saturations of 89%–92%. Finally, when the full saturation is reached (100%), the dispersion and the corresponding attenuation disappeared. In this last case, the Young’s modulus increases to a value of 40.5 GPa to compare with a Young modulus of 38 GPa at dry condition.

Figures 6c and 6d present the frequency-dependent Poisson’s ratio at different water saturations. The relative uncertainty on ν is around $\Delta \nu/\nu = 4\%$, which corresponds to 0.01 for ν . For saturation lower than 75%, the Poisson’s ratio is independent of frequencies in the range of 0.01–100 Hz, and the corresponding Poisson’s phase difference is negligible. However, as the water saturations increase from 75% to 99%, there is an obvious dispersion and at a saturation of 89%. Poisson’s ratio increases from 0.25 to 0.30 as the frequencies increase from 20 to 100 Hz. This transition moves toward lower frequency as the saturation increases. The corresponding Poisson’s ratio phase difference behaves consistently with the dispersion, that is, the attenuation peaks appear at the frequencies of 20–100 Hz, moving toward lower frequency with increasing saturation. In addition, the

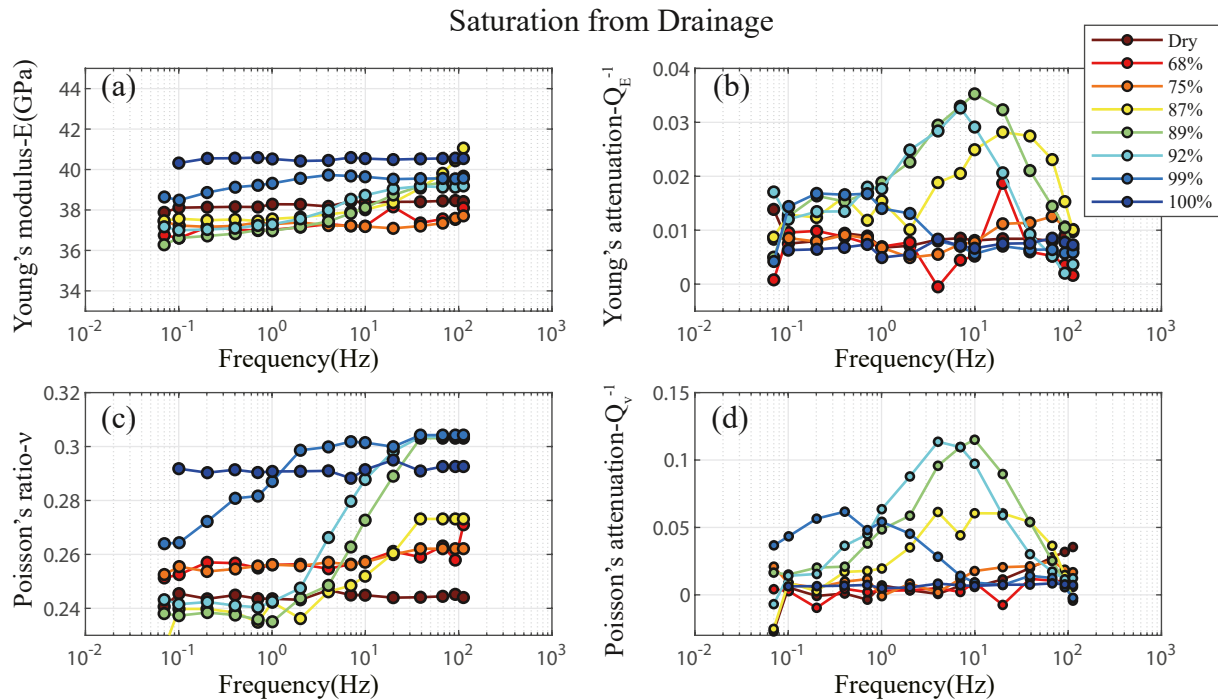


Figure 6. Young's modulus (a), Young's attenuation (b), Poisson's ratio (c), and Poisson's attenuation (the phase difference between the radial strain and the axial strain) measured using the oscillation method as the water saturation increases from dry to 100% by drying method. The relative uncertainty of the Young's modulus is around 5%, and the uncertainty of Poisson's ratio is around 4%.

magnitude of the Poisson's ratio phase difference increases to the maximum of 0.12 at saturations of 89%–92%. Finally, when the full saturation is reached (100%), the dispersion and the corresponding attenuation disappeared.

Young's moduli (E and Q_E^{-1}) and Poisson's ratio (ν and Q_ν^{-1}) were used to deduce S wave moduli (G and Q_G^{-1}) and bulk moduli (K and Q_K^{-1}), which are shown in Figure 7. Propagating the uncertainties of E and ν to K and G , we obtained an uncertainty of 6.4% for K and G , which correspond to 1.6 GPa for K and 0.9 GPa for G . In addition, the ultrasonic measurements (G and K) are presented in Figure 6 (stars) with an error of $\pm 2\%$. When the saturations are lower than 75%, there is no dispersion and attenuation for the bulk moduli in the frequencies of 0.01–100 Hz. However, at the saturation of 75%, there is an offset between the bulk modulus measured at 100 Hz (45 GPa) and at 1 MHz (50 GPa). When the saturations reach 87%–99%, dispersion and attenuation of the bulk modulus appear in the frequencies of 0.01–100 Hz, and for these saturation the measurements at 100 Hz are consistent with those obtained at 1 MHz.

The attenuation peaks move toward lower frequencies as the water saturation increases. The magnitude of the attenuation peak is maximum at a saturation of 89%. When the water saturation is 100%, the dispersion and attenuation disappeared. Comparing with the bulk moduli, the G (shear modulus) presents negligible dispersion and attenuation in the frequencies of 0.01–1 MHz for all the water saturations. That means the fluid saturation has no influence on the shear modulus, which is consistent with most previous measurements regarding the partial saturations (Chapman et al., 2016; Spencer & Shine, 2016).

3.3. Bulk Modulus Versus Saturation and Frequency

The bulk moduli measurements versus saturation are presented in Figure 8. Figure 8a corresponds to the saturations of 65%, 88%, 94%, and 100%, obtained by the imbibition method. Figure 8b corresponds to the saturations of 68%, 75%, 87%, 89%, 92%, 99%, and 100%, obtained by the drainage method. Different colors mean different frequencies, that is, 0.4, 7, 10, 39, and 68 Hz. The red stars in Figures 8a and 8b are the ultrasonic results using the drainage method and the imbibition method. The two black lines—two limits corresponding to two extreme states of the fluid at low frequency and high frequency—are calculated using Gassmann–Hill (GH) and Gassmann–Wood (GW) prediction (Müller et al., 2010).

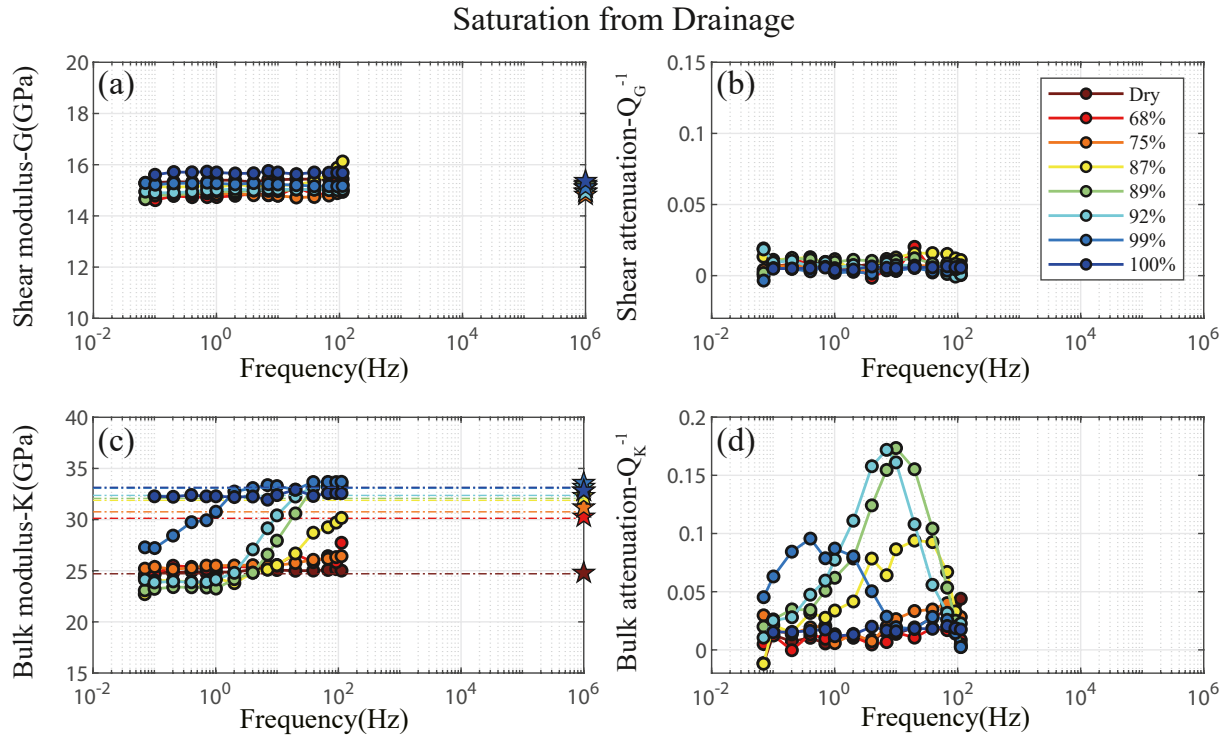


Figure 7. S wave modulus (a), S wave attenuation (b), bulk modulus (c), and bulk attenuation (d) are deduced from Figure 6. The circles are the low-frequency measurement and the stars are the ultrasonic measurements. The colorful dash lines are the Gassmann–Hill predictions at water saturations of 0%, 68%, 75%, 87%, 89%, 92%, 99%, and 100%. The relative uncertainties of (a)–(d) are 6.4%.

The “GW limit” refers to the case that the fluid has enough time (corresponding to sufficiently low frequency) to flow and equilibrate the pore pressure. Therefore, the mixed fluid can be regarded as a single phase and its effective fluid bulk modulus K_f can be calculated using Wood (1946):

$$K_f = \left(\frac{S_{WAT}}{K_{WAT}} + \frac{S_{AIR}}{K_{AIR}} \right)^{-1} \quad (11)$$

where S and K refer to the saturation and bulk modulus, respectively. The subscripts f , WAT , and AIR refer to the biphasic fluid, water, and air, respectively. There are only two phases in the saturated sample, so, $S_{WAT} + S_{AIR} = 1$. Putting K_f into Gassmann (1951)’s formula (Equation 12), one can get GW limit of an undrained sample saturated with two fluids.

$$K_u = K_d + \frac{\left(1 - \frac{K_d}{K_s}\right)^2}{\frac{\phi}{K_f} + \frac{1-\phi}{K_s} - \frac{K_d}{K_s^2}} \quad (12)$$

where ϕ , K_u , K_d , K_s , and K_f correspond respectively to porosity, the bulk moduli of the undrained sample, the drained sample, the solid matrix, and the pore fluid.

On the other hand, “GH limit” refers to the case that the fluid has no time (corresponding to sufficiently high frequency) to flow and behaves like a solid. The separate fluid phases are effectively isolated such that Gassmann’s formula (Equation 13) can be used to define an undrained bulk modulus for each region saturated by the respective fluid. Subsequently, an effective bulk modulus for the entire sample can be defined by applying Hill (1963)’s law:

$$K_{GH} = \left(\frac{S_{AIR}}{K_{AIR} + \frac{4G_d}{3}} + \frac{S_{WAT}}{K_{WAT} + \frac{4G_d}{3}} \right)^{-1} - \frac{4}{3}G_d \quad (13)$$

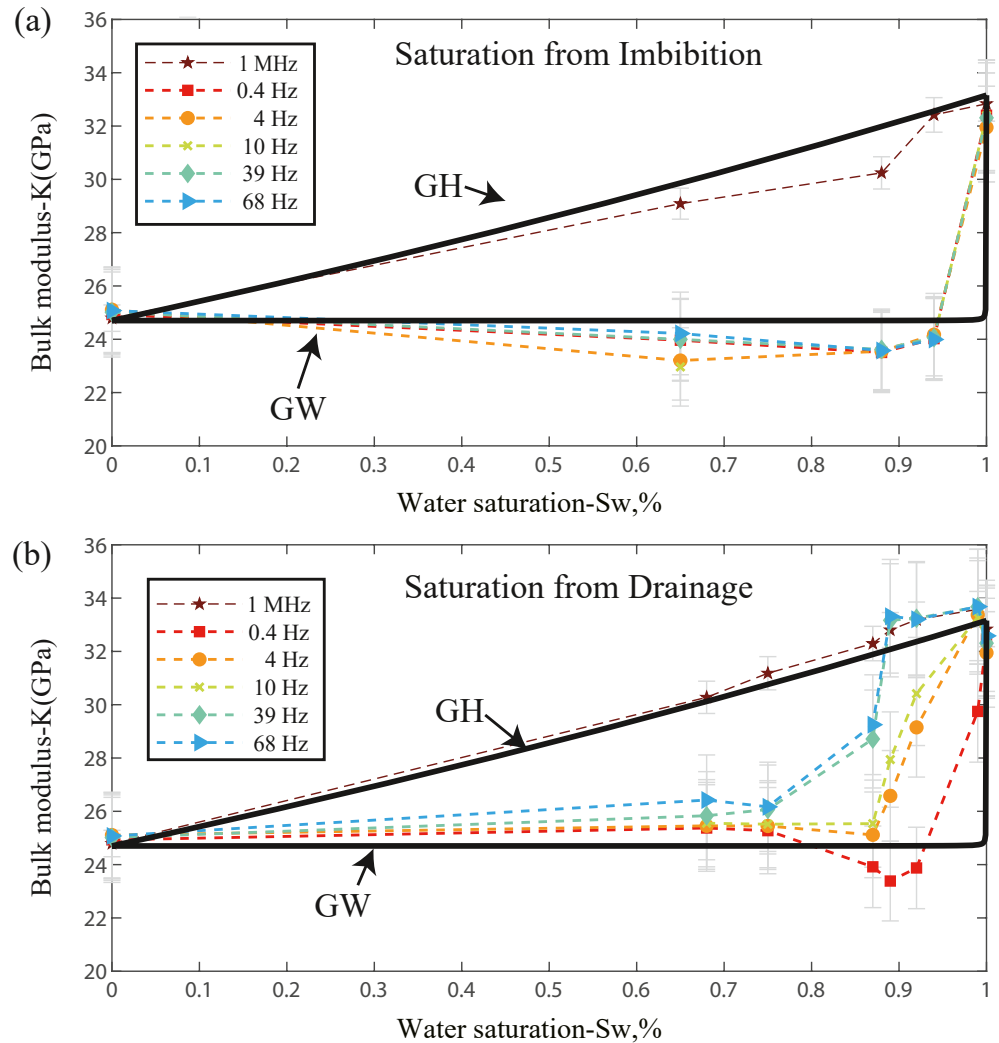


Figure 8. Bulk modulus versus the saturations at the frequency of [0.4 Hz, 7 Hz, 10 Hz, 39 Hz, 68 Hz, 1 MHz]. The relative uncertainty is 6.4% for the low-frequency measurement and 2% for the ultrasonic measurement. (a) From the Imbibition method and (b) from the Drainage method.

where K_{AIR} and K_{WAT} are the undrained bulk modulus of the portions of the sample saturated only by air and water, respectively (Mavko & Mukerji, 1998). G_d is the shear modulus for drained sample.

At the first order, Figure 8 shows that the low-frequency (below 100 Hz) measurements are close to the GW prediction, especially for the fluid distributions obtained from imbibition (Figure 8a); whereas, the ultrasonic measurements are close to the GH prediction for saturation higher than 60%, in agreement with the results on sandstone reported by Lebedev et al. (2009). In more detail, the low-frequency moduli (below 100 Hz) corresponding to the drainage distributions are always higher than the GW prediction and get closer to the GH prediction as the saturation increased from 87% to 92% (Figure 8b). As the saturation reaches values close to full saturation (>99%), the bulk moduli obtained by the different methods reach a value of 32 GPa, in agreement with GH and GW predictions.

3.4. Porosity and Fluid Distribution

Fluid distribution is a key parameter to interpret the measured dispersion and attenuation. To investigate the fluid distribution, the sample at four saturation scenarios (dry, full saturation, and 88% water saturation with imbibition and drainage method) were scanned (Section 2.5). The results are shown in Figure 9. Porosity and gas saturation

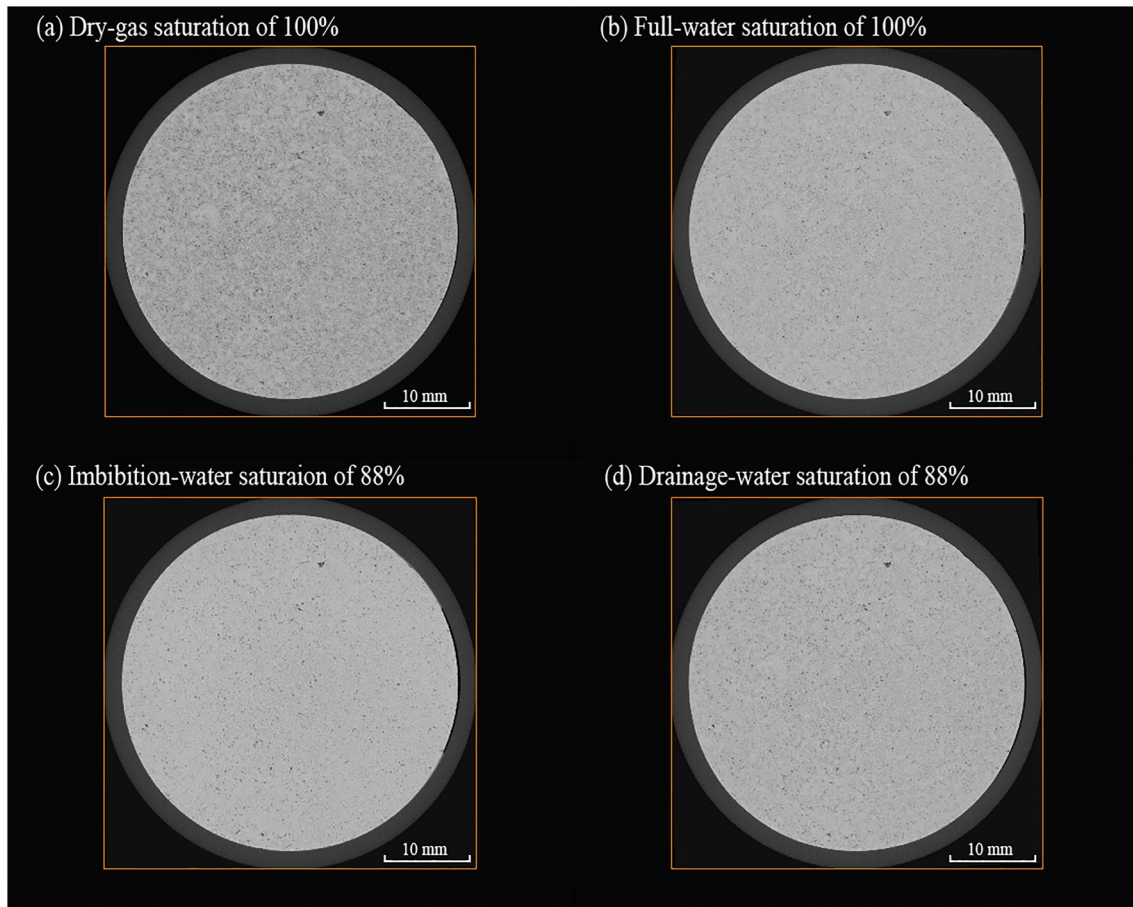


Figure 9. Reconstructed X-ray CT cross section of the central cross section of the volume shown in Figure 3 under different conditions: dry sample (a), water-saturated sample (b), and partially water-saturated sample (saturation of 88%) obtained by imbibition (c) and drainage (d) method. The resolution of the scans is $22 \mu\text{m}$.

maps are calculated from Equations 8 and 9 using the gray values in the images of the air-saturated (Figure 9a), water-saturated (Figure 9b), and partially water-saturated sample (imbibition, Figure 9c; drainage, Figure 9d).

The calculated porosity is shown in Figure 10. Here, the distribution of the porosity is homogeneous (Figures 10b–10d give the views in the XY , XZ , and YZ sections) and the averaged porosity is found to be 10%, which is in agreement with the one measured using triple-weight method in Section 2.3.

The saturation maps are shown in Figures 11 and 12 for the imbibition and drainage methods, respectively. In both cases, the saturation is 88%. Comparing Figures 11 and 12, the sizes of the gas patch are much bigger in the drainage case than in the imbibition case. In addition, the gas distribution is relatively homogeneous for imbibition case (Figures 11b–11d), whereas for the drainage case, gas patches seem to be concentrated at the boundaries of the sample (Figures 12c and 12d), where evaporation may be enhanced during the drying process (Section 2.4).

4. Theoretical Considerations Based on WIFF

According to Borgomano et al. (2019), there is no dispersion related to squirt-flow in this Indiana sample. This conclusion is also confirmed by our experiments as no dispersion is observed between seismic and ultrasonic measurements when the sample is fully saturated (Figures 6 and 7). Therefore, patchy saturation (White et al., 1975) seems to be the main reason causing attenuation and dispersion in our experiment.

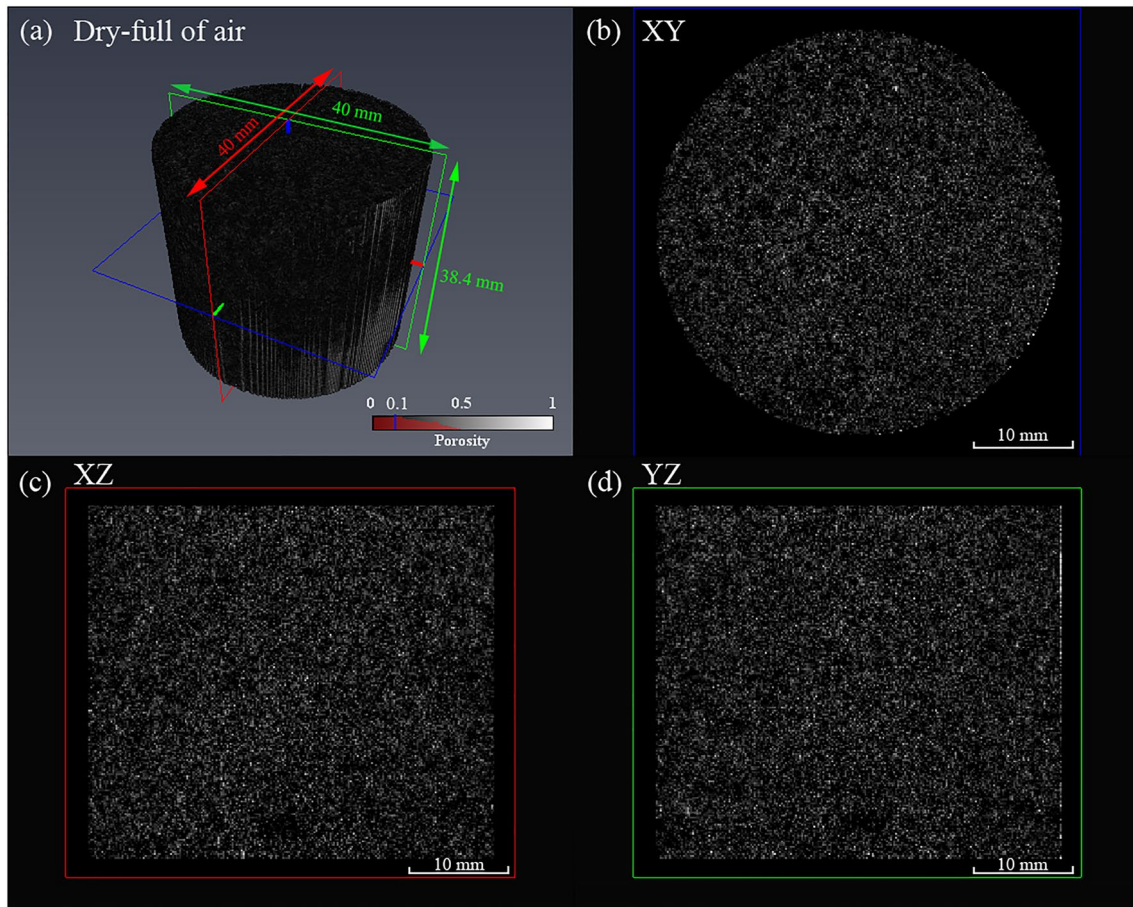


Figure 10. (a) 3D porosity distribution for dry sample Indiana. The slices are the porosities for the XY section (b), XZ section (c), and YZ section (d). The porosity is reconstructed from the dry and water-saturated CT scanning results. The voxel dimensions are $(0.176 \times 0.176 \times 0.176)$ mm³. The red area in porosity colormap legend means histogram of the grayscale. Noting that most gray values focus on 10%, which is consistent with porosity measurement.

4.1. Critical Frequency Predicted by Random Patchy Saturation Model

Müller and Gurevich (2004) gives an analytical solution for a patchy-saturated medium assuming a 1D random patchy saturation model. Based on this model, the critical frequency is

$$f_{patchy} = \frac{\kappa N}{2\pi\eta a^2} \quad (14)$$

where κ is the permeability of the sample; a is the correlation length, which is a measure of the length scale of heterogeneity (Müller et al., 2008). η is the fluid viscosity. $N = \frac{ML}{H}$, with $L = K_{dry} + \frac{4}{3}G_{dry}$ and $H = K_{sat} + \frac{4}{3}G_{dry}$; L and H are the dry and saturated P wave moduli, respectively. In the framework of the poroelasticity (e.g., Wang, 2000), $K_{sat} = K_{dry} + \alpha^2 M$, with $M = \left(\frac{[\alpha - \phi]}{K_s} + \frac{\phi}{K_f} \right)^{-1}$ and α is the Biot's coefficient defined as $\alpha = 1 - \frac{K_{dry}}{K_s}$. K_{dry} , K_{sat} , and K_s are the dry, saturated, and grain bulk modulus, respectively. G_{dry} is the dry shear modulus. In our experiment, ϕ , κ , K_s , K_{dry} , G_{dry} , and η are known and equal to 10.8%, 2×10^{-17} m², 77 GPa, 25 GPa, 15.2 GPa, and 1.10–3 Pa s, respectively. For a water saturation of 88%, the correlation length a was roughly estimated using a Debye correlation function (Toms-Stewart et al., 2009). For the drainage case, a is around 1.7 mm which leads to a critical frequency of around ~ 17 Hz according to Equation 14. It is closed to our experimental results where a peak of attenuation was observed around 20 Hz (light blue circles in Figure 6). For the imbibition case, a is around 0.8 mm for a saturation of 88%, which corresponds to a critical frequency of around 80 Hz. This is a bit different from our experimental results (light blue circles in Figure 5): no dispersion was observed in the range of 0.1–100 Hz, but dispersion was observed between 100 Hz and 1 MHz. The discrepancies could be from: (a) our rough estimation on the length a , as the critical frequency (Equation 14)

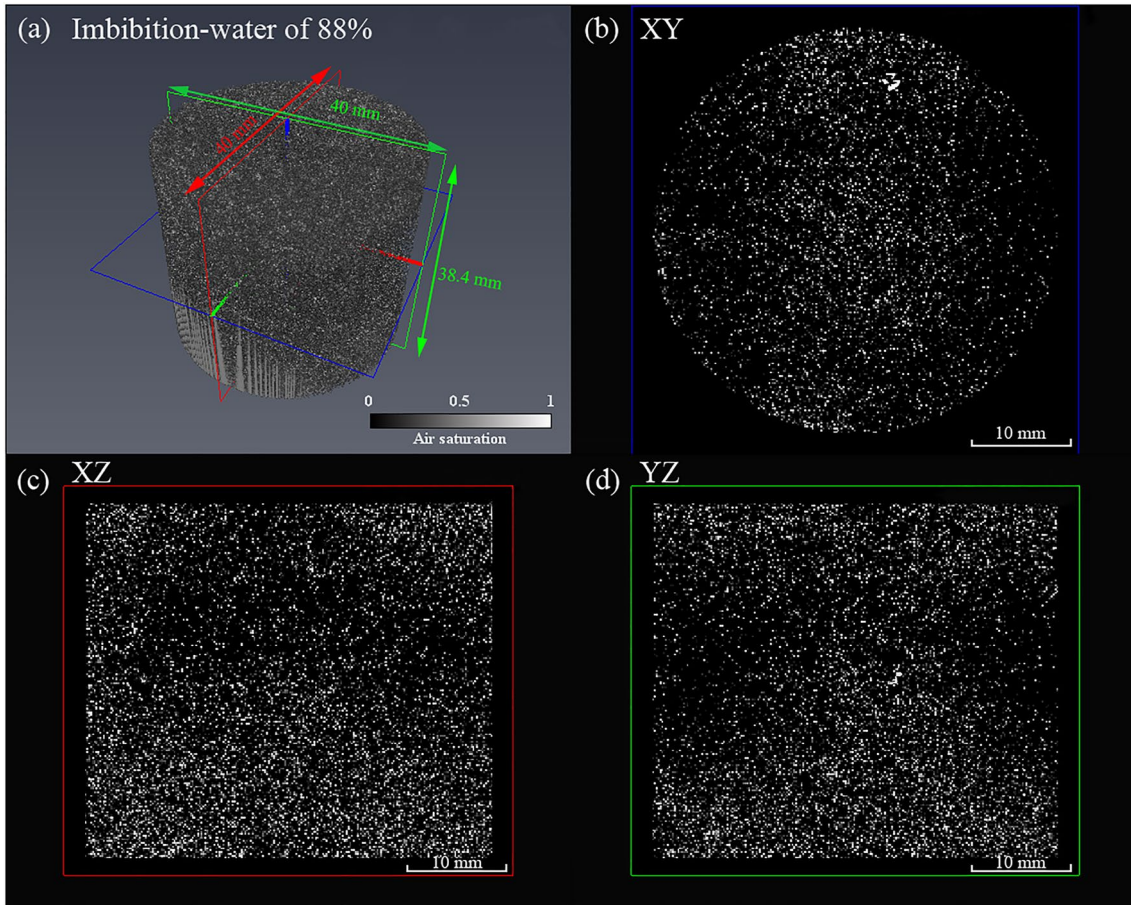


Figure 11. (a) 3D fluid distribution for the imbibition case at a water saturation of 88%. The slices are the fluid distribution for the XY section (b), XZ section (c), and YZ section (d). The voxel dimensions are $(0.176 \times 0.176 \times 0.176) \text{ mm}^3$.

depends on a^2 ; (b) the assumption done in the model that the patches are randomly distributed. In order to better estimate the dispersion and attenuation of elastic moduli, we used in the next section, a numerical model based directly on the fluid distribution obtained through the CT scan.

4.2. The Prediction of Numerical Method on Dispersion and Attenuation

Following Rubino et al. (2009), Biot's equation (Biot, 1956a, 1956b, 1962) in space-frequency domain can be summarized as follows:

$$-\omega^2 \mathbf{P}u(\mathbf{x}, \omega) + i\omega \mathbf{B}u(\mathbf{x}, \omega) - \mathbf{L}(u(\mathbf{x}, \omega)) = 0 \quad (15)$$

where $u = [u^s, u^f]$ is the displacement vector consisting of the solid (u^s) and fluid (u^f) phases, \mathbf{x} is the coordinate in cartesian system, ω is the angular frequency. The matrix \mathbf{P} in the equation is the matrix related to the density of matrix and fluid:

$$\mathbf{P} = \begin{pmatrix} \rho_b \mathbf{I} & \rho_f \mathbf{I} \\ \rho_f \mathbf{I} & g \mathbf{I} \end{pmatrix} \quad (16)$$

where \mathbf{I} denotes the identity matrix, ρ_b is the density of fluid-saturated sample, and ρ_f is the fluid density. By definition,

$$\rho_b = (1 - \phi)\rho_s + \phi\rho_f \quad (17)$$

where ρ_s is the density of the dry matrix and ϕ is the porosity.

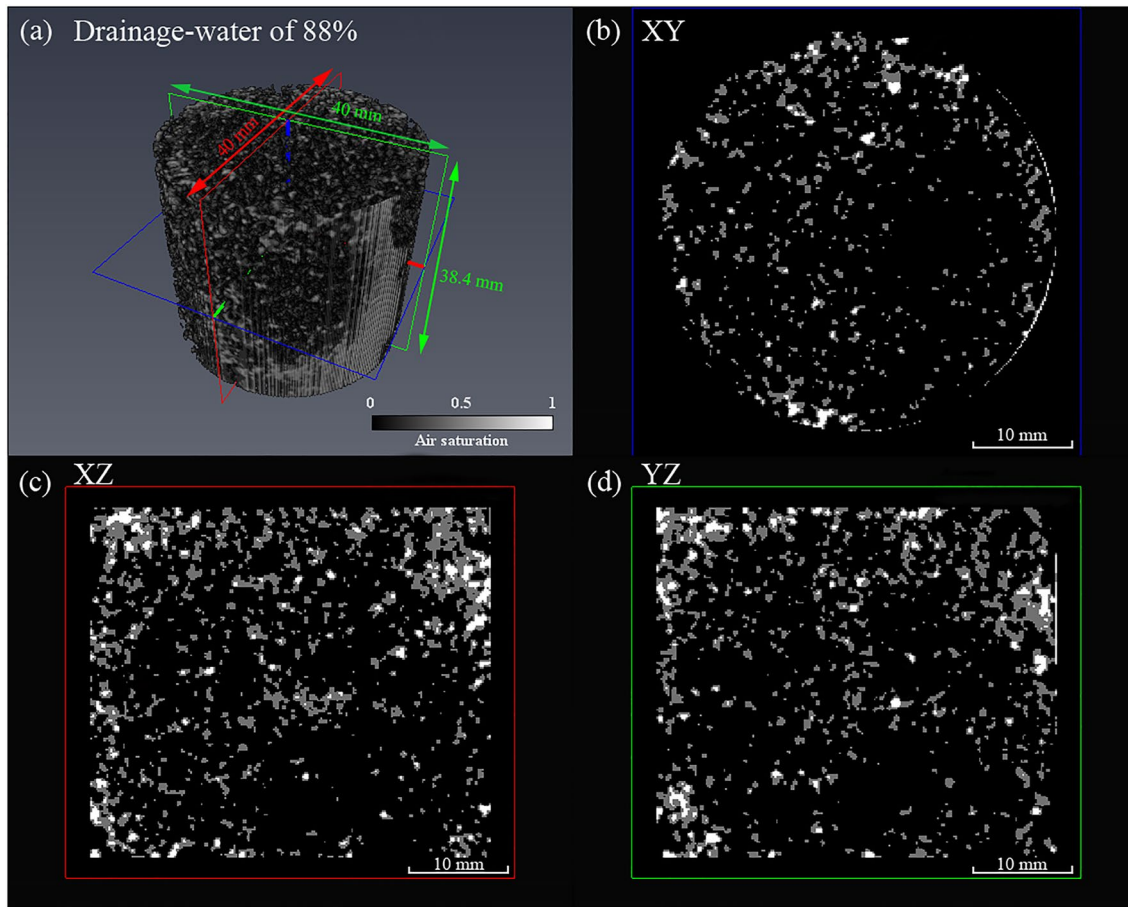


Figure 12. (a) 3D fluid distribution for the drainage case at a water saturation of 88%. The slices are the fluid distribution for the XY section (b), XZ section (c), and YZ section (d). The voxel dimensions are $(0.176 \times 0.176 \times 0.176)$ mm³.

B is the matrix related to the viscosity and permeability:

$$\mathbf{B} = \begin{pmatrix} 0\mathbf{I} & 0\mathbf{I} \\ 0\mathbf{I} & b\mathbf{I} \end{pmatrix} \quad (18)$$

And

$$b = \frac{\eta}{k}, \quad g = \frac{S\rho_f}{\phi}, \quad S = \frac{1}{2} \left(1 + \frac{1}{\phi} \right) \quad (19)$$

where η is the fluid viscosity, k is the permeability, and S is the tortuosity factor. **L** is the second-order differential operator defined by (Rubino et al., 2009)

$$\mathbf{L}(u) = (\nabla \cdot \boldsymbol{\sigma}(u), -\nabla p_f(u))^t \quad (20)$$

where $\boldsymbol{\sigma}$ is the stress tensor and p_f is the pore pressure of fluid.

The fluid saturation is implicitly contained in the matrix (Equation 16) and (Equation 18) of Equation 15. To solve Equation 15, we specify the boundary condition (red lines in Figure 13a) as the Plane-Wave boundary condition: that is $\varepsilon_{xx} = 0$ for a 2D case or $\varepsilon_{xx} = \varepsilon_{xy} = \varepsilon_{yy} = \varepsilon_{yx} = 0$ for a 3D case. The P wave modulus is defined as

$$M = \sigma_{zz} / \varepsilon_{zz} \quad (21)$$

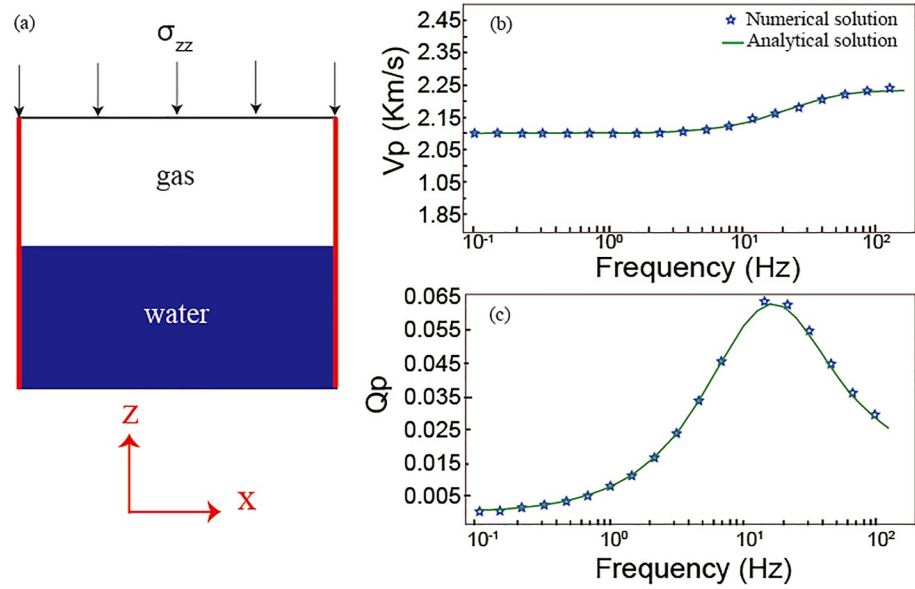


Figure 13. Numerical experiment of the White's model. (a) White's model for a water saturation of 50%. An axial oscillation stress σ_{zz} is loaded on the boundary of the sample. P wave velocity (b) and P wave attenuation (c) calculated using the numerical model (blue stars) and the analytical solution (green line).

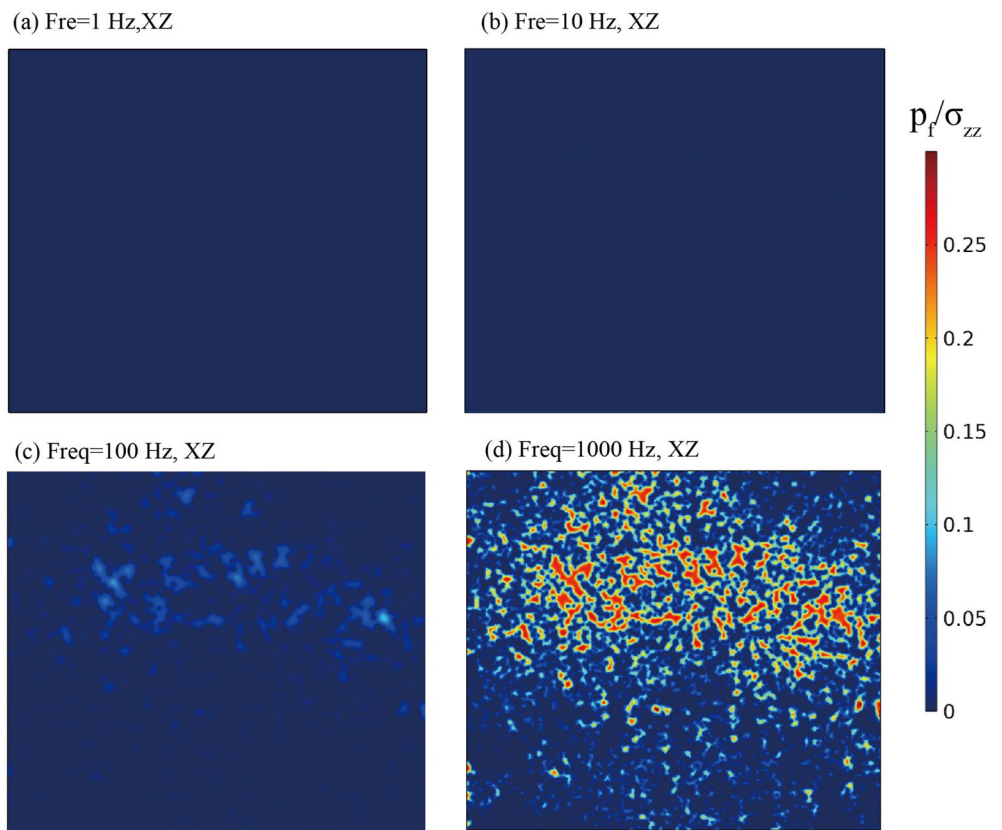


Figure 14. The ratio of fluid pressure to loading stress, at frequencies of (a) 1 Hz, (b) 10 Hz, (c) 100 Hz, and (d) 1,000 Hz, for imbibition method at the water saturation of 88%. They are predicted using the numerical model in Section 4.2 combining the fluid distribution of X-Z section in Figure 11c.

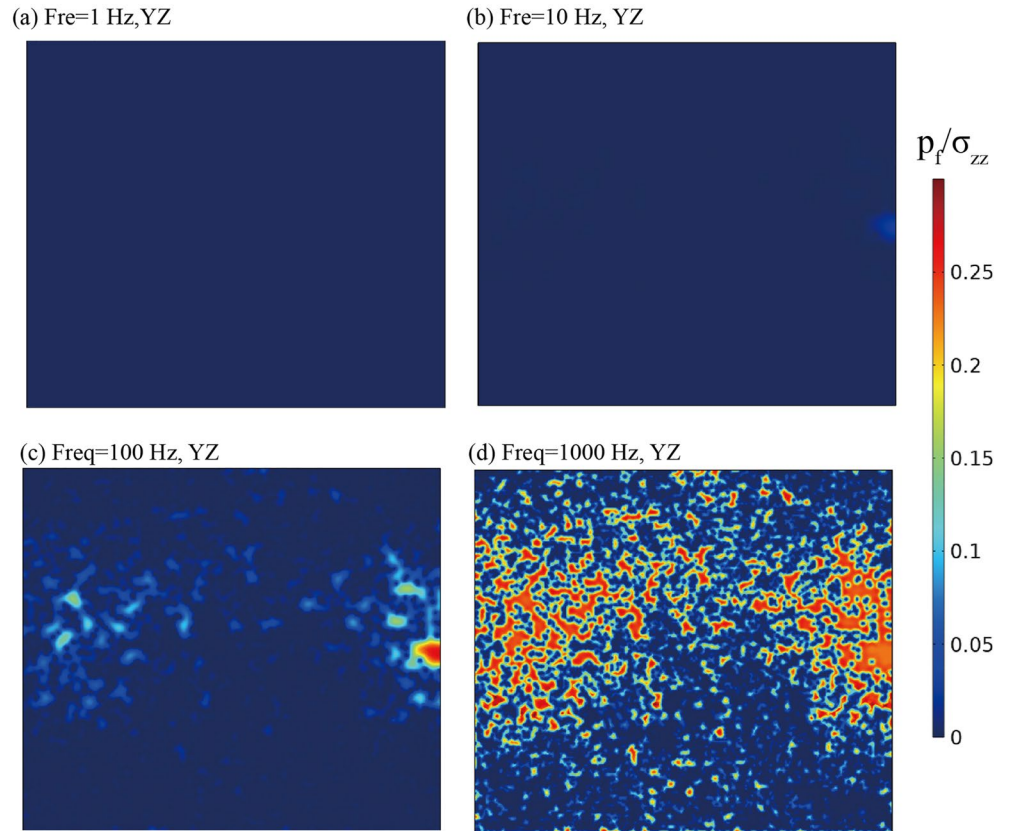


Figure 15. The ratio of fluid pressure to loading stress, at frequencies of (a) 1 Hz, (b) 10 Hz, (c) 100 Hz, and (d) 1,000 Hz, for imbibition method at the water saturation of 88%. They are predicted using the numerical model in Section 4.2 combining the fluid distribution of Y–Z section in Figure 11d.

where σ_{zz} is an axial-stress oscillation stress loading on the up boundary (Figure 13a), and ε_{zz} is the vertical strain. The fluid is not allowed to flow into or out of the sample. The P wave velocity V_p and P wave attenuation Q_p can be calculated as

$$V_p = \sqrt{\frac{M}{\rho_b}}, \quad Q_p = \frac{\Im(V_p)}{\Re(V_p)} \quad (22)$$

where \Im and \Re are the Imagery and Real operator. The numerical model is first tested in the case of a layer model (saturation of 50%), for which White et al. (1975) gave an analytical solution. Figures 13b and 13c show for this case the predictions of P wave velocity and attenuation. The numerical solution (blue stars) fits perfectly the analytical solution (green solid line).

4.3. Numerical Prediction of Dispersion and Attenuation Based on Fluid Distribution From CT

A numerical prediction (Equations 15 and 20) could be carried out using the finite element method, using a 3D fluid distribution (Figure 11 or 12) as an input. However, meshing such small 3D patches is time consuming and request a large random-access-memory (RAM) for calculation, at least 100 GB. Considering the calculation ability available, we decided to perform a 2D numerical modeling using the 2D sections (Figures 11 and 12).

Figures 14 and 15 show the numerical prediction of the water pressure when a P wave propagates through the partially saturated limestone at different frequencies. These results are given for a saturation of 88% after the imbibition: the cross section XZ of Figure 11c is used as an input for the numerical results obtained in Figure 14; whereas the cross section YZ is used as an input for the numerical results obtained in Figure 15. At frequencies of 1, 10, and 100 Hz, the water pressure is almost 0: at these frequencies, excess of water pore pressure induced by

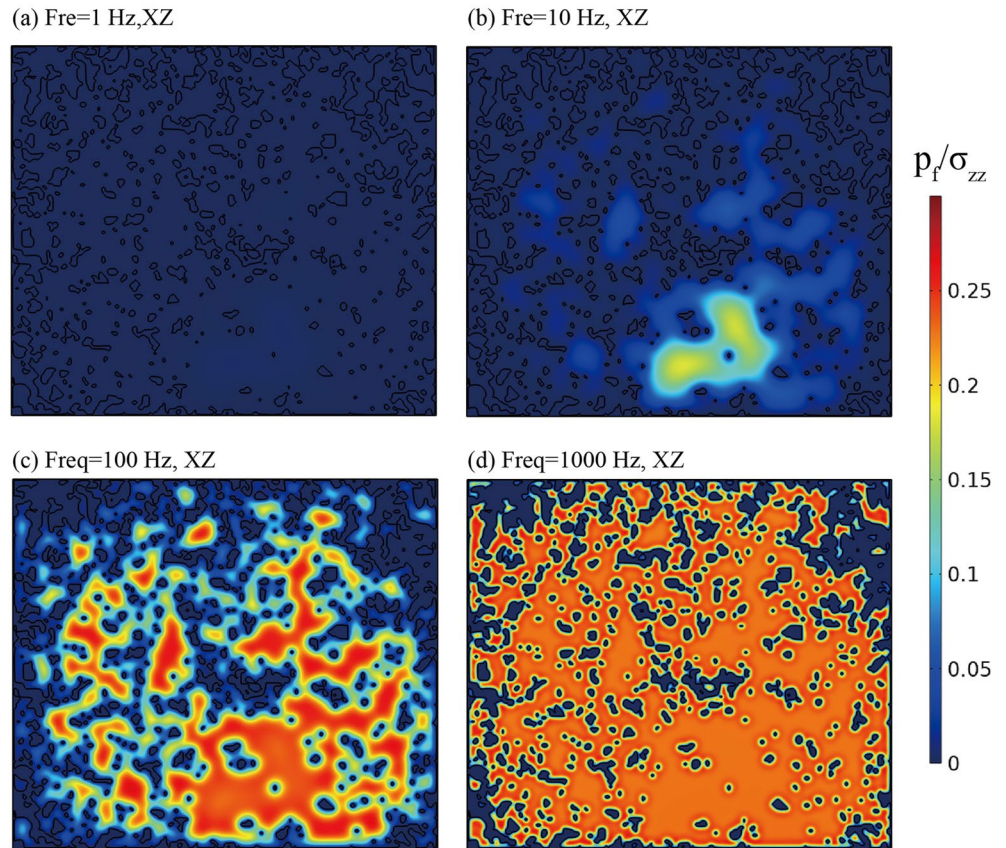


Figure 16. The ratio of fluid pressure to loading stress, at frequencies of (a) 1 Hz, (b) 10 Hz, (c) 100 Hz, and (d) 1,000 Hz, for drainage method at the water saturation of 88%. They are predicted using the numerical model in Section 4.2 combining the fluid distribution of X–Z section in Figure 12c.

the P wave has the time to equilibrate with the gas pocket (mesoscopic flow), that is, the fluid pressure is relaxed and gas and water pressure are equilibrated. However, as the frequency increases from 100 Hz to 1 kHz, several patches of pressurized water occur (Figure 14d), that is, the water pressure does not have time to diffuse through the gas pocket. The variation of the fluid pressure explains that there is no dispersion and attenuation of the bulk modulus for frequency <100 Hz but a dispersion between 100 Hz and 1 MHz, this is in agreement with our experimental results (Figures 4 and 5). Figure 18 compares our experimental results obtained on the bulk modulus and its attenuation for a saturation of 88% using the imbibition method (cross dots) with the 2D numerical predictions (dashed red and green lines), with the CT scan used as an input for the fluid distribution. Overall, there is a good consistency, and the absence of attenuation in our experimental results for frequency <100 Hz is explained by a homogeneous distribution of small gas pockets (with size ≤ 1 mm).

Figures 16 and 17 show the numerical prediction of the water pressure in the case of drainage for different frequencies. These results are given for a saturation of 88%: the cross section XZ of Figure 12 is used as an input for the numerical results obtained in Figure 16; whereas the cross section YZ is used as an input for the numerical results obtained in Figure 17. At a frequency of 1 Hz, the water pressure is almost 0 (Figures 16 and 17a), that is, the fluid pressure is relaxed and gas and water pressure are equilibrated. As the frequency increases from 10 to 1,000 Hz, patches of pressurized water occur, which is different from the imbibition case. At a frequency of 1 kHz, almost all the water inside the rock is pressurized (Figures 16 and 17d). The numerical simulation based on the fluid distribution obtained from the CT scan confirmed the existence of a bulk dispersion and attenuation in for frequency >1 Hz. Figure 18 compares our experimental results obtained on the bulk modulus and its attenuation for a saturation of 88% using the drainage method (square dots) with the 2D numerical predictions (red and green lines). The numerical predictions of the bulk modulus match well with the measurements: the match is good in terms of dispersion and frequency cutoff. Regarding the attenuation, the match between the numerical

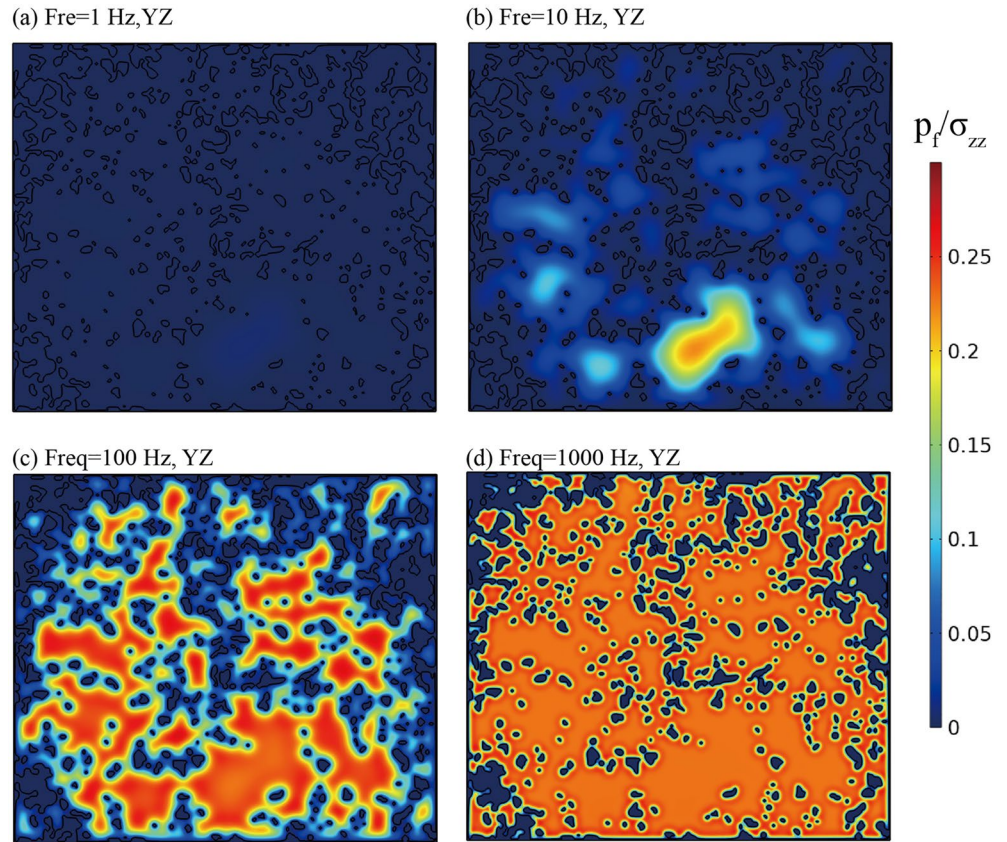


Figure 17. The ratio of fluid pressure to loading stress, at frequencies of (a) 1 Hz, (b) 10 Hz, (c) 100 Hz, and (d) 1,000 Hz, for drainage method at the water saturation of 88%. They are predicted using the numerical model in Section 4.2 combining the fluid distribution of Y – Z section in Figure 12d.

results and experimental data is good in terms of frequency, nevertheless, there is a slight discrepancy between the measured and modeled attenuation values, the modeled attenuations are always smaller than the measurements. The discrepancy is above the uncertainty of the measured attenuation (0.01) and is probably due to the use of a 2D section instead of a 3D volume, between which there maybe differences in fluid saturation and distribution.

5. Conclusions

In this paper, we investigated experimentally the impact of a partial saturation on the attenuation and dispersion of elastic-wave velocities. The experiments were performed on an Indiana limestone, partially saturated (water/air) using two methods: imbibition and drainage. Dispersion and attenuation of elastic moduli were measured under pressure using the forced-oscillation method in the range of 0.1–100 Hz, while the fluid distributions were investigated under CT scan.

In the case of drainage, our experimental results show that a clear peak of attenuation was observed at a frequency of ~ 20 Hz as the saturation increases from 68% to 100%, these results are correlated with an increase of the elastic moduli and the P wave velocity. In the case of imbibition, dispersion was observed but for frequency between 100 Hz and 1 MHz. The same saturation obtained during drainage or imbibition leads to different results in terms of dispersion and attenuation and thus highlights the effect of fluid distribution on the dispersion and attenuation of elastic-wave velocities.

To better understand our experimental results, we performed CT scans on samples saturated by imbibition and drainage and show that drainage leads to a more heterogeneous distribution of the fluid with bigger air patches. We first interpret our experimental results in the light of White's model: larger patch induces a lower critical

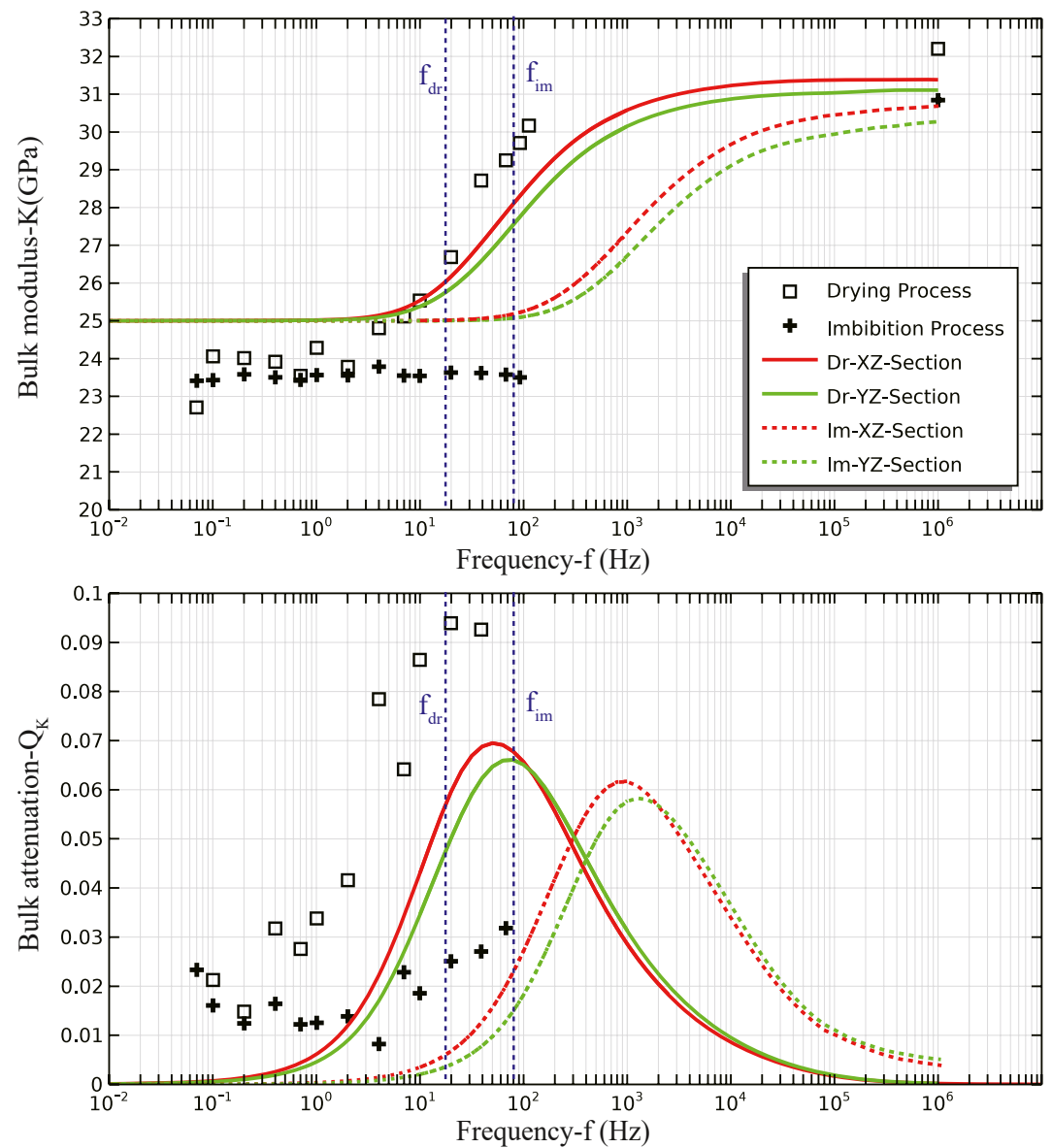


Figure 18. The bulk modulus (a) and the bulk attenuation (b) varying with the frequencies. They are composed of measurements (square dots and plus dots) and numerical predictions (solid and dash lines in red and green). The dots obtained at the frequency of 106 Hz are deduced from the ultrasonic measurements. The measurements are from the saturation case of 88% for imbibition and 87% for drainage. f_{dr} and f_{im} are the critical frequencies estimated using formula 14.

frequency cutoff. But a critical parameter needed for the White's model is the mean size of the patch. To overcome this difficulty, we used a numerical model based on Biot's theory and used the CT scanning results as a constrained input for the fluid distribution.

We found that the numerical predictions obtained by the poroelastic theory match well with the measurements. In addition, the numerical simulation provides the possibility to quantify the relationship between fluid distribution and seismic attenuation and could be a useful tool for upscaling at reservoir scale.

Data Availability Statement

Data sets are available online (<https://doi.org/10.5281/zenodo.5525026>).

Acknowledgments

This work is supported by National Natural Science Foundation of China (42104111, 41930425, 41725017, 41774143, and 41804104); National Key R&D Program of the Ministry of Science and Technology of China (2020YFA0713400); State Key Laboratory of Petroleum Resources and Prospecting, China University of Petroleum.

References

- Akin, S., & Kovscek, A. R. (2003). Computed tomography in petroleum engineering research. *Geological Society, London, Special Publications*, 215(1), 23–38. <https://doi.org/10.1144/GSL.SP.2003.215.01.03>
- Biot, M. A. (1956a). Theory of propagation of elastic waves in a fluid-saturated porous solid. I. Low-frequency range. *Journal of the Acoustical Society of America*, 28(2), 168–178. <https://doi.org/10.1121/1.1908239>
- Biot, M. A. (1956b). Theory of propagation of elastic waves in a fluid-saturated porous solid. II. Higher frequency range. *Journal of the Acoustical Society of America*, 28(2), 179–191. <https://doi.org/10.1121/1.1908241>
- Biot, M. A. (1962). Mechanics of deformation and acoustic propagation in porous media. *Journal of Applied Physics*, 33(4), 1482–1498. <https://doi.org/10.1063/1.1728759>
- Borgomano, J. V. M., Gallagher, A., Sun, C., & Fortin, J. (2020). An apparatus to measure elastic dispersion and attenuation using hydrostatic- and axial-stress oscillations under undrained conditions. *Review of Scientific Instruments*, 91(3), 034502. <https://doi.org/10.1063/1.5136329>
- Borgomano, J. V. M., Pimienta, L., Fortin, J., & Guéguen, Y. (2017). Dispersion and attenuation measurements of the elastic moduli of a dual-porosity limestone. *Journal of Geophysical Research: Solid Earth*, 122, 2690–2711. <https://doi.org/10.1002/2016JB013816>
- Borgomano, J. V. M., Pimienta, L. X., Fortin, J., & Guéguen, Y. (2019). Seismic dispersion and attenuation in fluid-saturated carbonate rocks: Effect of microstructure and pressure. *Journal of Geophysical Research: Solid Earth*, 124, 12498–12522. <https://doi.org/10.1029/2019JB018434>
- Cadoret, T. (1993). *Effet de la Saturation Eau/Gaz sur les Propriétés Acoustiques des Roches* (Ph.D. dissertation). Paris: University of Paris VII.
- Cadoret, T., Marion, D., & Zinszner, B. (1995). Influence of frequency and fluid distribution on elastic wave velocities in partially saturated limestones. *Journal of Geophysical Research*, 100(B6), 9789–9803. <https://doi.org/10.1029/95JB00757>
- Chapman, S., Borgomano, J. V. M., Quintal, B., Benson, S. M., & Fortin, J. (2021). Seismic wave attenuation and dispersion due to partial fluid saturation: Direct measurements and numerical simulations based on X-ray CT. *Journal of Geophysical Research: Solid Earth*, 126, e2021JB021643. <https://doi.org/10.1029/2021JB021643>
- Chapman, S., Borgomano, J. V. M., Quintal, B., Benson, S. M., & Fortin, J. (2022). Mass transfer between fluids as a mechanism for seismic wave attenuation: Experimental evidence from water–CO₂ saturated sandstones. *Geophysical Journal International*, 230(1), 216–234. <https://doi.org/10.1093/gji/ggac067>
- Chapman, S., Tisato, N., Quintal, B., & Holliger, K. (2016). Seismic attenuation in partially saturated Berea sandstone submitted to a range of confining pressures. *Journal of Geophysical Research: Solid Earth*, 121, 1664–1676. <https://doi.org/10.1002/2015JB012575>
- Domenico, S. N. (1976). Effect of brine–gas mixture on velocity in an unconsolidated sand reservoir. *Geophysics*, 41(5), 882–894. <https://doi.org/10.1190/1.1440670>
- Dutta, N., & Odé, H. (1979). Attenuation and dispersion of compressional waves in fluid-filled porous rocks with partial gas saturation (White model)—Part I: Biot theory. *Geophysics*, 44(11), 1777–1788. <https://doi.org/10.1190/1.1440938>
- Fossum, A. F., Senseny, P. E., Pfeifle, T. W., & Mellegard, K. D. (1995). Experimental determination of probability distributions for parameters of a Salem limestone cap plasticity model. *Mechanics of Materials*, 21(2), 119–137. [https://doi.org/10.1016/0167-6636\(95\)00002-X](https://doi.org/10.1016/0167-6636(95)00002-X)
- Gassmann, F. (1951). Über die elastizität poröser medien: Vier. der Natur. *Gesellschaft Zürich*, 96, 1–23.
- Geertsma, J. (1961). Velocity-log interpretation: The effect of rock bulk compressibility. *Society of Petroleum Engineers Journal*, 1(04), 235–248. <https://doi.org/10.2118/1535-G>
- Geremia, D., David, C., Ismail, R., & El Haitami, A. (2021). An integrated study of water weakening and fluid rock interaction processes in porous rocks: Linking mechanical behavior to surface properties. *Applied Sciences*, 11(23), 11437. <https://doi.org/10.3390/app112311437>
- Hart, D. J., & Wang, H. F. (1995). Laboratory measurements of a complete set of poroelastic moduli for Berea sandstone and Indiana limestone. *Journal of Geophysical Research*, 100(B9), 17741–17751. <https://doi.org/10.1029/95JB01242>
- Hill, R. (1963). Elastic properties of reinforced solids: Some theoretical principles. *Journal of the Mechanics and Physics of Solids*, 11(5), 357–372. [https://doi.org/10.1016/0022-5096\(63\)90036-X](https://doi.org/10.1016/0022-5096(63)90036-X)
- Hirschwald, J. (1912). *Handbuch der bautechnischen Gesteinsprüfung für Beamte der Materialprüfungsanstalten und Baubehörden, Steinbruchingenieure*. In *Architekten und Bauingenieure: sowie für Studierende der technischen Hochschulen* (Vol. 2). Stuttgart: Gebrüder Borntraeger.
- Ji, Y., Baud, P., Vajdova, V., & Wong, T.-f. (2012). Characterization of pore geometry of Indiana limestone in relation to mechanical compaction. *Oil & Gas Science and Technology – Revue d'IFP Energies Nouvelles*, 67(5), 753–775. <https://doi.org/10.2516/ogst/2012051>
- Knight, R., & Dvorkin, J. (1992). Seismic and electrical properties of sandstones at low saturations. *Journal of Geophysical Research*, 97(B12), 17425–17432. <https://doi.org/10.1029/92JB01794>
- Lebedev, M., Toms-Stewart, J., Clennell, B., Pervukhina, M., Shulakova, V., Paterson, L., et al. (2009). Direct laboratory observation of patchy saturation and its effects on ultrasonic velocities. *The Leading Edge*, 28, 24–27. <https://doi.org/10.1190/1.3064142>
- Lin, Q., Bijeljic, B., Rieke, H., & Blunt, M. J. (2017). Visualization and quantification of capillary drainage in the pore space of laminated sandstone by a porous plate method using differential imaging X-ray microtomography. *Water Resources Research*, 53, 7457–7468. <https://doi.org/10.1002/2017WR021083>
- Masschaele, B., Dierick, M., Van Loo, D., Boone, M. N., Brabant, L., Pauwels, E., et al. (2013). Hector: A 240kV micro-CT setup optimized for research. *Journal of Physics: Conference Series*, 463, 012012. <https://doi.org/10.1088/1742-6596/463/1/012012>
- Mavko, G., & Mukerji, T. (1998). Bounds on low-frequency seismic velocities in partially saturated rocks. *Geophysics*, 63(3), 918–924. <https://doi.org/10.1190/1.1444402>
- Michalopoulos, L. P., & Triandafilidis, G. E. (1976). Influence of water on hardness, strength and compressibility of rock. *Environmental and Engineering Geoscience*, xiii(1), 1–22. <https://doi.org/10.2113/gseegeosci.xiii.1.1>
- Müller, T. M., & Gurevich, B. (2004). One-dimensional random patchy saturation model for velocity and attenuation in porous rocks. *Geophysics*, 69(5), 1166–1172. <https://doi.org/10.1190/1.1801934>
- Müller, T. M., Gurevich, B., & Lebedev, M. (2010). Seismic wave attenuation and dispersion resulting from wave-induced flow in porous rocks—A review. *Geophysics*, 75(5), A147–A164. <https://doi.org/10.1190/1.3463417>
- Müller, T. M., Toms-Stewart, J., & Wenzlau, F. (2008). Velocity-saturation relation for partially saturated rocks with fractal pore fluid distribution. *Geophysical Research Letters*, 35, L09306. <https://doi.org/10.1029/2007GL033074>
- Murphy, W. F., III. (1982). *Effects of microstructure and pore fluids on the acoustic properties of granular sedimentary materials* (Ph.D. dissertation). Stanford, CA: Stanford University.
- Pimienta, L., Borgomano, J. V. M., Fortin, J., & Guéguen, Y. (2016). Modelling the drained/undrained transition: Effect of the measuring method and the boundary conditions: Modelling drained/undrained transition. *Geophysical Prospecting*, 64(4), 1098–1111. <https://doi.org/10.1111/1365-2478.12390>
- Pride, S. R., Berryman, J. G., & Harris, J. M. (2004). Seismic attenuation due to wave-induced flow. *Journal of Geophysical Research*, 109, B01201. <https://doi.org/10.1029/2003JB002639>

- Qi, Q., Tobias, M. M., & Boris, G. (2014). Quantifying the effect of capillarity on dispersion and attenuation in patchy-saturated rocks. *Geophysics*, 79(5), WB35–WB50. <https://doi.org/10.1190/geo2013-0425.1>
- Qi, Q., Tobias, M. M., & Germán, R. (2014). Seismic attenuation: Effect of interfacial impedance on wave-induced pressure diffusion. *Geophysical Journal International*, 199, 1677–1681. <https://doi.org/10.1093/gji/ggu327>
- Rubino, J. G., & Holliger, K. (2013). Research note: Seismic attenuation due to wave-induced fluid flow at microscopic and mesoscopic scales: Microscopic and mesoscopic effects. *Geophysical Prospecting*, 61(4), 882–889. <https://doi.org/10.1111/1365-2478.12009>
- Rubino, J. G., Ravazzoli, C. L., & Santos, J. E. (2009). Equivalent viscoelastic solids for heterogeneous fluid-saturated porous rocks. *Geophysics*, 74(1), N1–N13. <https://doi.org/10.1190/1.3008544>
- Solazzi, S. G., Guarracino, L., Rubino, J. G., & Holliger, K. (2019). Saturation hysteresis effects on the seismic signatures of partially saturated heterogeneous porous rocks. *Journal of Geophysical Research: Solid Earth*, 124, 11316–11335. <https://doi.org/10.1029/2019JB017726>
- Spencer, J. W. (1981). Stress relaxations at low frequencies in fluid-saturated rocks: Attenuation and modulus dispersion. *Journal of Geophysical Research*, 86(B3), 1803–1812. <https://doi.org/10.1029/JB086iB03p01803>
- Spencer, J. W., & Shine, J. (2016). Seismic wave attenuation and modulus dispersion in sandstones. *Geophysics*, 81(3), D211–D231. <https://doi.org/10.1190/geo2015-0342.1>
- Sun, C., Tang, G., Zhao, J., Zhao, L., Long, T., Li, M., & Wang, S. (2019). Three-dimensional numerical modelling of the drained/undrained transition for frequency-dependent elastic moduli and attenuation. *Geophysical Journal International*, 219(1), 27–38. <https://doi.org/10.1093/gji/ggz284>
- Tiennot, M., & Fortin, J. (2020). Moisture-induced elastic weakening and wave propagation in a clay-bearing sandstone. *Géotechnique Letters*, 10(3), 424–428. <https://doi.org/10.1680/jgele.19.00052>
- Tisato, N., & Madonna, C. (2012). Attenuation at low seismic frequencies in partially saturated rocks: Measurements and description of a new apparatus. *Journal of Applied Geophysics*, 86, 44–53. <https://doi.org/10.1016/j.jappgeo.2012.07.008>
- Tisato, N., & Quintal, B. (2013). Measurements of seismic attenuation and transient fluid pressure in partially saturated Berea sandstone: Evidence of fluid flow on the mesoscopic scale. *Geophysical Journal International*, 195(1), 342–351. <https://doi.org/10.1093/gji/ggt259>
- Toms-Stewart, J., Müller, T. M., Gurevich, B., & Paterson, L. (2009). Statistical characterization of gas-patch distributions in partially saturated rocks. *Geophysics*, 74(2), WA51–WA64. <https://doi.org/10.1190/1.3073007>
- Tutuncu, A. N. (1992). *Velocity dispersion and attenuation of acoustic waves in granular sedimentary media (Ph.D. dissertation)*. Austin, TX: University of Texas.
- Vajdova, V., Baud, P., & Wong, T. (2004). Compaction, dilatancy, and failure in porous carbonate rocks. *Journal of Geophysical Research*, 109, B05204. <https://doi.org/10.1029/2003JB002508>
- Wang, H. F. (2000). *Theory of linear poroelasticity with applications to geomechanics and hydrogeology*. Princeton, NJ: Princeton University Press. <https://doi.org/10.1515/9781400885688>
- White, J. E., Mihailova, N., & Lyakhovitsky, F. (1975). Low-frequency seismic waves in fluid-saturated layered rocks. *Journal of the Acoustical Society of America*, 57(S1), S30. <https://doi.org/10.1121/1.1995164>
- Winkler, K., & Nur, A. (1979). Pore fluids and seismic attenuation in rocks. *Geophysical Research Letters*, 6(1), 1–4. <https://doi.org/10.1029/GL006i001p00001>
- Wood, A. B. (1946). *A textbook of sound* (2nd ed.). New York: MacMillan. Retrieved from <http://archive.org/details/in.ernet.dli.2015.15768>
- Yin, H., Borgomano, J. V. M., Wang, S., Tiennot, M., Fortin, J., & Guéguen, Y. (2019). Fluid substitution and shear weakening in clay-bearing sandstone at seismic frequencies. *Journal of Geophysical Research: Solid Earth*, 124, 1254–1272. <https://doi.org/10.1029/2018JB016241>
- Zhu, W., Baud, P., & Wong, T. (2010). Micromechanics of cataclastic pore collapse in limestone. *Journal of Geophysical Research*, 115, B04405. <https://doi.org/10.1029/2009JB006610>